

Supporting Information

Regulating *OCCHO intermediate pathway towards high selective photocatalytic CO₂ reduction to CH₃CHO over locally crystallized carbon nitride

Qiong Liu^a[⁺], Hui Cheng^a[⁺], Tianxiang Chen^b, Tsz Woon Benedict Lo^b, Zhangmin Xiang^a, and Fuxian Wang^{a*}

^aInstitute of Analysis, Guangdong Academy of Sciences (China National Analytical Center, Guangzhou), Guangzhou, Guangdong, 510070, China

^bState Key Laboratory of Chemical Biology and Drug Discovery, Department of Applied Biology and Chemical Technology, The Hong Kong Polytechnic University, Hong Kong, China

*E-mail: wangfuxian@fenxi.com.cn (F. Xian).

[⁺] These authors contributed equally to this work.

Table of Contents

1. Experimental Procedures.....	3
2. Supplementary Note.....	9
3. Figures and discussions.....	12
4. Tables	40
5. References.....	52

1. Experimental Procedures

1.1. Materials

Dicyandiamide ($C_2H_4N_4$, $\geq 99.0\%$), amino-2-propanol (C_3H_9NO , $\geq 99.8\%$), triethanolamine (TEOA, analytical reagent), ethanol (C_2H_5OH , $\geq 99.7\%$), Acetonitrile (MeCN, 99.9%) was purchased from Macklin Chemical. Deuterium oxide (D_2O , 99.9%) was purchased from Energy Chemical. Acetaldehyde (CH_3CHO , standard for GC, 99.5%) and Formaldehyde solution (HCHO, analytical standard) were purchased from Aladdin Bio-Chem Technology Co.,LTD. High purity argon (Ar, $\geq 99.99\%$), carbon dioxide (CO_2 , $\geq 99.9999\%$), and Carbon- ^{13}C dioxide ($^{13}CO_2$, $\geq 99\%$), Carbon dioxide- $^{18}O_2$ ($C^{18}O_2$, $\geq 99\%$) was provided by Air Liquide. 5,5-dimethyl-1-pyrroline-N-oxide (DMPO) were purchased from Sigma Aldrich Chemical Co. All materials were used without further purification.

1.2. Sample synthesis

Synthesis of HCN-A: All chemicals used are reagent grade purity. In a typical synthesis, 10 g of dicyandiamide (DCDA) was added into 50 mL deionized water with a certain amount of amino-2-propanol (AP) and stirred for 30 min at 80 °C. Then mixture suspension was transferred to a 100 mL stainless steel autoclave and heated at 180 °C. After cooling to the ambient temperature, the obtained pale yellow suspension was filtered and washed by using water and ethanol for three times, thoroughly dried at 100 °C in a vacuum oven. The resulted solids were loaded in a 50 ml ceramic crucible, subjected to the thermal pyrolysis treatment at 550 °C for 4 h in a Nabertherm muffle furnace at 7 °C/min. After cooling down, the loosely packed yellow solids of polymeric carbon nitride (PCN) were obtained, yielding 1.6-1.8 g. This polymeric carbon nitride sample via the hydrothermal treatment and AP modification named as HCN-A. These obtained HCN-A samples modified by different concentration addition of AP, such as 0.1, 0.2, 0.5, and 1.0 mL, denoted as HCN-A₁, HCN-A₂, HCN-A₃, and HCN-A₄.

Synthesis of HCN: For comparison, a bulk PCN sample was synthesized from DCDA by the directly calcined in a muffle furnace by using the identical experimental conditions (550 °C/4 h~7 °C/min), denoted CN. And the porous PCN sample via the hydrothermal treatment just without the addition of AP, and then endured the identical calcination process was denoted as HCN.

1.3. General information for Instrumental details

Scanning electron microscopy (SEM) was performed on a Field Emission Hitachi SU8220 electron microscope. Transmission electron microscopy (TEM) was performed with a JEM-2100 JEOL electron microscope (200 kV). The thickness of the sample was measured by Bruker Multimode 8 Atomic force microscopy (AFM). X-ray diffraction (XRD) patterns were collected using a Bruker D8 advance X-ray powder diffractometer (Cu K α 1) over a 2 θ range of 5-60 with Bragg-Brentano geometry. Fourier transforms infrared (FT-IR) spectra were recorded on Bruker Vector 33 FTIR infrared spectrophotometer with the range of 4000-400 cm⁻¹. For X-ray photoelectron spectroscopy (XPS), the sample was pressed onto indium foil and monitored on a Thermo Fisher Scientific K-Alpha X-ray photoelectron spectrometer. The spectra were referenced to the adventitious C 1s peak at 284.80 eV. Magic Angle Spinning (MAS) solid-state ¹³C nuclear magnetic resonance (NMR) spectra were carried out by an Agilent 600 MHz PremiumCOMPACT NMR magnet system with a rotate rate of 8 k. Analysis of nitrogen adsorption-desorption isotherms were performed at liquid nitrogen temperature and the CO₂ absorption curve was detected at 298 K on a Micromeritics ASAP 2020 apparatus, samples were degassed for 10 h at 150 °C before the sorption measurements. Specific surface areas were calculated using Brunauer-Emmett-Teller (BET) theory. CNH elemental analyses were acquired by an Elementar Vario MICRO cube. Thermogravimetric analysis was performed with the Netzsch GmbH STA 409 CD. The synchrotron X-ray absorption near-edge structure (XANES) measurements for the C and N K-edge were performed at BL20A beamline in the Singapore Synchrotron Light Source, Singapore.

Diffuse reflectance UV-Vis spectra (DRS) were recorded on a Hitachi U-4100 spectrophotometer, referenced to barium sulfate. The spectra in percentage reflectance were converted by using the Kubelka-Munk function, the optical band gaps were extracted assuming direct transition from these spectra. Static photoluminescence (PL) emission spectra (370 nm excitation) were acquired with a Horiba Scientific Aqualog Fluorescence spectrometer. Time-resolved fluorescence decay spectra were conducted on an Edinburgh PLS980 fluorescence spectrometer with a time-correlated single photon counting (TCSPC) system. Ultraviolet photoelectron spectroscopy (UPS) analysis was recorded by a Ulvac-PHI 5000 VersaProbe III SCA photoelectron spectrometer, He I (21.22 eV) as the monochromatic discharge photon source, and a bias potential of -5 V was applied to monitor the secondary electron

cutoff. The sample was pressed into a flat film and stained to the surface of conductive tape, while the side of the conductive tape was fixed on the instrument stage. The cutoff energy was measured based on the intersection between the linear extrapolation of the cutoff region and the baseline.

MS and MS/MS analysis were performed on a Thermo Scientific Q Exactive Orbitrap Velos Pro equipped with an electrospray ionization (ESI) source. The tested samples were injected to MS instrument with a flow rate of 10 mL min⁻¹. The test intermediates were achieved as follows: 10 g of dicyandiamide (DCDA) with the 0.5 mL AP addition endured the hydrothermal pretreatment, after cooling to the room temperature, the suspension was then filtered by a 0.22 μm filter to get a clarified aqueous solution. The final solution was used for MS analysis.

High-resolution X-ray diffraction (XRD) patterns were collected with a Rigaku SmartLab diffractometer (3 kW X-ray tube, equipped with Mo X-ray anode) in the 2θ range of 3-30° with 0.001° data binning with a 0.5 mm borosilicate glass holder. Each pattern was collected by applying a very slow speed of 0.4° min⁻¹ for 60 min in total. This procedure produced good quality patterns with the high signal-to-noise ratio. The X-ray total scattering data was acquired from Rigaku Smartlab diffractometer (3kW, equipped with Mo X-ray anode) for PDFgui refinement of finite-size NCs. This was collected by scattering signals over the 2θ range of 3-150° using a 0.5 mm borosilicate capillary glass holder. It is capable of measuring a maximum Q-range of 17 Å⁻¹ and a typical measurement may last for about 3 hours for one sample. For XPDF data treatment, we used the Rigaku in-built software for the subtraction of air and capillary background. Note that data optimization was carefully treated through manual operation^[1].

Femtosecond transient absorption measurements (fs-TA) were monitored on a Helios pump-probe system (Ultrafast Systems LLC) together with a femtosecond amplified laser system (Coherent). The regenerative frequency-doubled optical parametric amplifier system (TOPAS-800-fs, 365 nm pump pulse) was separated to multiple light beams. One provides a Ti: sapphire amplifier 800 nm laser pulses to generate a certain wavelength goes through the sample and a second focused on the commercial pulsed diode-pumped Nd: YLF laser (Coherent Evolution-30) goes to the reference spectrometer to monitor the fluctuations in the probe beam intensity. The temporal delay was mounted by applying a motorized moving stage. The pump and probe pulses was overlapped spatially

to avoid anisotropy effects and the signal was collected by a pair of diode arrays detector. For the present experiments, the sample was pretreated to form a semitransparent aqueous suspension of 5 mg/mL, sealed in a 1mm cuvette under a magnetic stirring condition and excited a 400 nm pump beam. The lifetimes of the photo-chemically induced reactive intermediates were achieved by fitting the spectrum using double-exponential functions.

In situ diffuse reflectance infrared Fourier transform spectroscopy (DRIFTS) measurement was conducted on Thermo Fisher Nicolet IS50 II FTIR spectrometer over the range of 4000 to 650 cm^{-1} at a resolution of 8 cm^{-1} . 5 mg of the powder catalyst samples were compressed at the bottom of the in-situ Harrick IR cell, and then degassed for 2 h under Ar atmosphere at 120 °C to remove the adsorbed species before the photocatalytical experiments. After cooling down to the room temperature, 30 mL/min pure CO_2 gas was flowed into the specimen chamber carrying the reaction solution (TEOA/MeCN solvent) to saturate the surface absorption of catalyst. After 30 min, the equilibrium of CO_2 on the catalyst was reached and the IR signal under dark condition was recorded for comparison. A 50 W white LED light was employed as the light source. The DRIFTS spectra were collected after certain irradiation duration (e.g., 1 min, 2 min, 3min, 4 min, 5 min, 10 min, 15 min, 20 min, 25 min and 30 min).

In-situ electron paramagnetic resonance (EPR) spectroscopy was carried out by the Bruker model A 300 spectrometer with the the light source of a 300 W Xe-lamp ($\lambda > 420$ nm). The active radical was captured by using the probe molecule DMPO, of which produced in a suspension of HCN-A catalyst in a TEOA (10%) /MeCN solvent and 10 wt% H_2O . EPR experimental conditions were set as: microwave frequency 9.85 GHz, microwave power was 19.82 mW, modulation frequency 100 kHz, modulation amplitude 1 G, field center 3510 G. The EPR spectra were collected from the 0 min (dark time), 5 min and 10 min under the visible light illumination.

1.4. Evaluation of photocatalytic CO_2 reduction

Photocatalytic CO_2 reduction was conducted on a Beijing PerfectLight PCX-50C Multi-channel photochemical reaction system equipped with the 5 W white LED Slight panel. In a typical experiment, 15 mg of the synthesized photocatalyst was dispersed in 3 mL 10% triethanolamine (TEOA)/acetonitrile (MeCN) solution with 0.3 mL H_2O in a 60 mL sealed Flat quartz reactor. The

suspension was ultra-sonicated for 15 min to ensure the solids catalyst was uniformly dispersed in the MeCN solution. Argon was purged through the reactor for three times with an interval of 30S vacuumed/inflated to remove the residual air by using AC1000 Atmosphere controller, subsequently, filled into the pure CO₂ gas into the reactor for five times to achieve a CO₂-saturated suspension solution. Then the reactor was illuminated under the white LED lamp to drive the photocatalytic CO₂ conversion reaction, using a magnetic stirrer with the constant rotational velocity of 250 r/min. The reaction temperature was kept at 10 °C by a closed water circulation system throughout the whole experiment.

The liquid products were determined on a gas chromatograph with the flame ionization detector (FID) detector (RB-INOWAX, capillary column, H₂+Air carrier gas with a 1:10 rate of flow value) after reaction by injected 1 µL aliquots of the reaction solution. The liquid products and isotope experiment was further verified by using Agilent Technologies 7890B with 7250 Accurate-Mass Q-TOF GC/MS system. The gaseous components were also investigated by an FID detector (polymer pellet molecular sieve) equipped with a mechanized by gas chromatography and the generation of H₂ gas was simultaneously detected by the TCD detector (Ar carrier gas, molecular sieve 5 Å column). The target liquid products were also analyzed using the fresh reacted sample (0.1 mL) in 0.5 mL D₂O by 1H-NMR spectroscopy (Bruker Avance III HD 500 MHz) via a water suppression mode.

The amount of HCHO was analyzed by using the acetylacetone colour-development method. Specifically, 1.6 mL of the as-prepared 0.25% (v/v) acetylacetone solution was mixed with 2.4 mL of the liquid product supernatant in a glass bottle, and heated for 3 min in boiling water, then the yellow colour of the mixed solution could be investigated. Afterwards, a specific amount of solution was taken out and examine the UV-vis absorption spectrum by using a Hitachi U-4100 spectrophotometer. Through the absorbance intensity at 413 nm, the HCHO concentration was obtained. The preparation of 0.25% (v/v) acetylacetone solution was as follows. Ammonium acetate (25 g) was dissolved in deionized water (20 mL), 3 mL of acetic acid and 0.25 mL of acetylacetone (0.25 mL) were then added in sequence. Afterwards, the solution volume was diluted with water to 100 mL, and was stored in refrigerator with 2-6 °C.

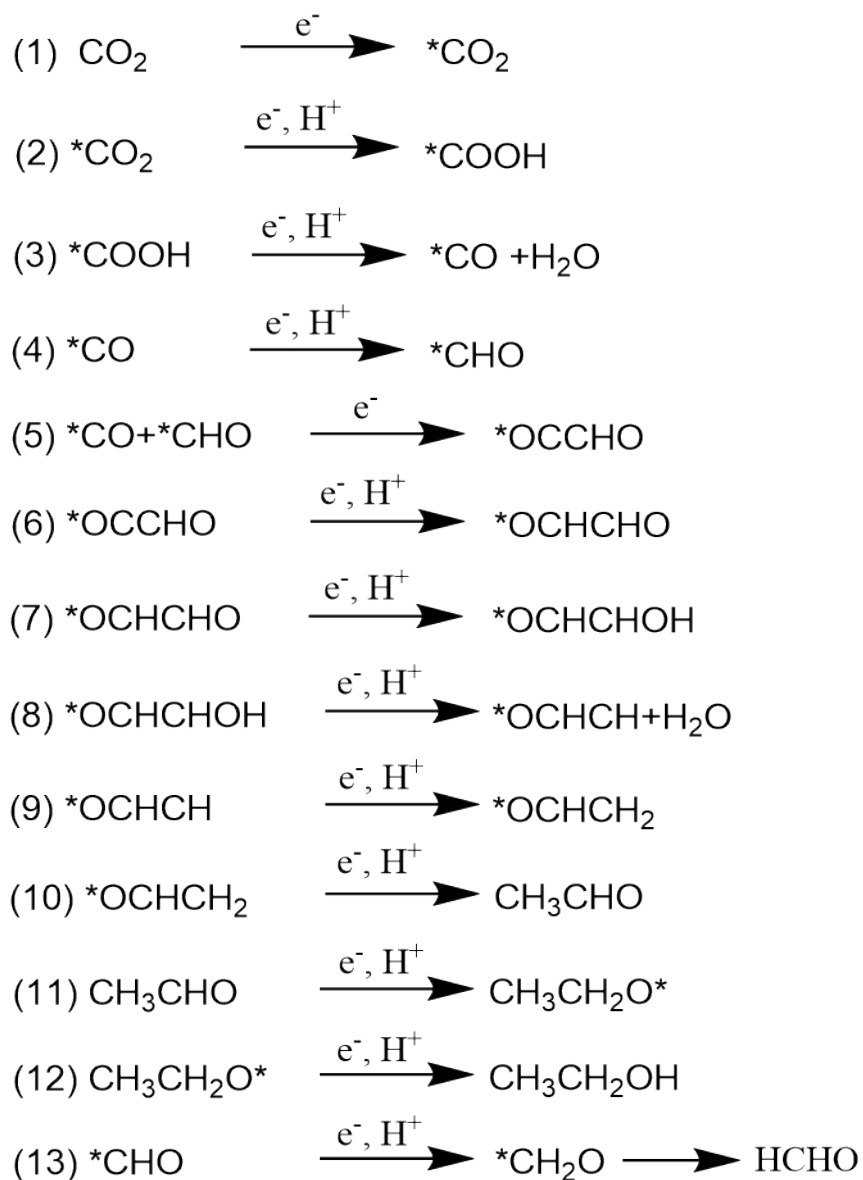
For stability tests, 15 mg catalyst was added in 3 mL 10% TEOA/acetonitrile solution with 0.3 mL H₂O, purged with pure CO₂, and irradiated by the LED light source. After 120 min, 1 μL aliquots was extracted for the analysis. Then the reaction suspension was filtered and washed for several times by using ethanol and H₂O. After thoroughly dried of the catalyst, the identical reaction system was conducted for the next 2 h illumination and further for the next subsequent 8 recycling runs.

1.5. Calculation of quantum efficiency (QE)

The quantum efficiency (QE) for CH₃CHO evolution was measured by using the Perfectlight PCX-50C Multi-channel photochemical reaction system under the illumination of the LED lamp. Different monochromatic wavelengths of light (λ) including 365±2 nm, 385±2 nm, 420±2 nm, 450±2 nm, 485±2 nm, 535±2 nm, 535±2 nm, and 630±2 nm was used as the light source. The amount of generated CH₃CHO was collected after 2 hours of light irradiation. Generally, the QE value under the different monochromatic wavelengths excitation were calculated by the following equation^[2]:

$$\begin{aligned} \text{QE}(\%) &= \frac{N_e}{N_p} = \frac{\text{number of reacted electrons}}{\text{number of incident photons}} \times 100\% \\ &= \frac{10 \times \text{number of evolved CH}_3\text{CHO molecules}}{\text{number of incident photons}} \times 100\% \quad (1) \end{aligned}$$

Note that reduction CO₂ to CH₃CHO is a ten-electrons transfer process, shown in the behinds^[3], that is to say, to generate one CH₃CHO molecule will consumed ten electrons.



1.6. Density functional theory (DFT) calculations

Plane-wave density functional theory (DFT) calculations were performed using the CASTEP module in Material Studio (MS) together with Vienna ab initio simulation package code (VASP)^[4]. The geometry structure of monolayer amorphous melon (PCN) model structure was optimized by the Perdew–Burke–Ernzerhof exchange–correlation functional of the generalized gradient approximation (GGA)^[5]. The spin-polarized GGA PBE exchange–correction functional and a projector augmented wave (PAW) method were employed, and a 520 eV cutoff energy was applied to the all-electron plane-wave basis sets for identifying the accuracy of the calculations^[6]. PCN is simulated by employing a triclinic model of P1 (2 × 2) unit cell periodicity based on the initial structure with crystal lattice parameters of

$\alpha=\beta=\gamma=90^\circ$. The Monkhorst-Pack grid was set as $3 \times 3 \times 1$ for PCN material to be the Brillouin-zone integrations. The vacuum slab of 15 Å was selected to eliminate the periodic interference of the unit cell. The conjugate gradient (CG) algorithm was adopted for the optimization. Partial occupancies of the Kohn–Sham orbitals were allowed using the Gaussian smearing method and a width of 0.05 eV. The electronic energy was considered self-consistent when the energy change was smaller than 10^{-5} eV. Grimme’s DFT-D3 methodology was used to describe the dispersion interactions^[7]. The reaction Gibbs energy change (ΔE) was calculated as follows:

$$\Delta E = E_{\text{total}} - E_{\text{sur}} - E_{\text{mol}} + \Delta E_{\text{ZPE}} - T\Delta S$$

where E_{total} is the total energy for the adsorption state, E_{sur} is the energy of the pure surface, E_{mol} is the energy of the molecule, ΔE_{ZPE} is the difference corresponding to zero-point energy and ΔS is the entropy change. Geometries of multiple configurations of each adsorbate locates on each available binding site were optimized into local energy minima (i.e. 0.05 eV/ Å). The most stable configuration selected for the energies shown in free energy diagram, with a free energy correction corresponding to vibrational contributions determined in the harmonic approximation was applied in every adsorbate.

2. Supplementary Note

Supplementary Note 1, quantum efficiency (QE) calculation

Take QE at the wavelength of 420 ± 2 nm of HCN-A as an example^[1a],

$$\begin{aligned} N_e &= \text{number of reacted electrons (mols}^{-1}\text{)} \\ &= 10 \times \frac{n}{t} = 10 \times \frac{23.071 \times 10^{-6}}{3600} = 6.409 \times 10^{-8} \text{ mols}^{-1} \end{aligned}$$

The number of CH_3CHO molecules can be calculated from the evolved rate of CH_3CHO under 420 nm ($23.071 \mu\text{mol h}^{-1}$). Then, the received electron number of the products (N_e) is $10 \times 23.071 \times 10^{-6} / 3600 = 6.409 \times 10^{-8} \text{ mols}^{-1}$.

The energy of a single photon (denoted as E_s) at $\lambda = 420$ nm is calculated to be 4.736×10^{-19} J, according to hc/λ (h and c are the Planck constant 6.63×10^{-34} J s and the speed of light 3×10^8 m/s, respectively).

$$E_s = \frac{hc}{\lambda} = \frac{6.63 \times 10^{-34} \times 3 \times 10^8}{4.2 \times 10^{-7}} = 4.736 \times 10^{-19} \text{ J}$$

The Avogadro's number (denoted as A) is 6.022×10^{23} . The light intensity (I) was measured as 20.9 mW/cm², which was calibrated by a light power meter (PL-MW2000). The diameter of the illumination window of the reactor was ~ 2.9 cm, corresponding to the irradiation area (S) of 6.60 cm². The total number of incident photons offered in the reaction vessel per hour (N_p) = 4.833×10^{-7} mol s⁻¹.

$$N_p = \frac{I \times S}{E_s \times A} = \frac{20.9 \times 10^{-1} \times 6.60 \times 10^{-4}}{4.736 \times 10^{-19} \times 6.022 \times 10^{23}} = 4.837 \times 10^{-7}$$

Thus, according to equation (1), the AQE (%) = 13.25%.

$$\begin{aligned} \text{AQE}(\%) &= \frac{N_e}{N_p} = \frac{\text{number of reacted electrons}}{\text{number of incident photons}} \times 100\% \\ &= \frac{6.409 \times 10^{-8}}{4.837 \times 10^{-7}} \times 100\% = 13.25\% \end{aligned}$$

Take AQY at the wavelength of 385 ± 2 nm of HCN-A as an other example,

The number of CH_3CHO molecules can be calculated from the evolved rate of CH_3CHO under 385 nm ($12.971 \mu\text{mol h}^{-1}$). Then, the received electron number of the products (N_e) is $10 \times 12.971 \times 10^{-6} / 3600 = 3.603 \times 10^{-8}$ mols⁻¹.

$$\begin{aligned} N_e &= \text{number of reacted electrons (mols}^{-1}\text{)} \\ &= 10 \times \frac{n}{t} = 10 \times \frac{12.971 \times 10^{-6}}{3600} = 3.603 \times 10^{-8} \text{ mols}^{-1} \end{aligned}$$

The energy of a single photon (denoted as E_s) at $\lambda = 385$ nm is calculated to be 5.166×10^{-19} J, the light intensity (I) was measured as 7.6 mW/cm². The total number of incident photons offered in the reaction vessel per hour (N_p) = 1.612×10^{-7} mol s⁻¹.

$$N_p = \frac{I \times S}{E_s \times A} = \frac{7.6 \times 10^1 \times 6.60 \times 10^{-4}}{5.166 \times 10^{-19} \times 6.022 \times 10^{23}} = 1.612 \times 10^{-7}$$

Thus, according to equation (1), the AQE (%) = 22.35%.

$$\begin{aligned} \text{AQE}(\%) &= \frac{N_e}{N_p} = \frac{\text{number of reacted electrons}}{\text{number of incident photons}} \times 100\% \\ &= \frac{3.603 \times 10^{-8}}{1.612 \times 10^{-7}} \times 100\% = 22.35\% \end{aligned}$$

Supplementary Note 2, Band position determination

The obtained UV-vis diffuse reflectance spectra (DRS) were first converted to absorption spectra according to the Kubelka-Munk function^[8],

$$F(R) = \frac{(1 - R)^2}{2R} \times 100\%$$

where R was the relative reflectance of samples with comparable to the reference. Then, the band gaps of samples were estimated from the basis of the Tauc equation,

$$F(R)hv = A(hv - E_g)^{\frac{n}{2}}$$

where h is Planck constant, ν is photon's frequency, A is a proportionality constant and E_g is the band gap energy, respectively, while n depends on the nature of electron transition in a semiconductor and is equal to $1/2$ or 2 for the direct and indirect transition, respectively. The values of E_g were determined from the plot of $(F(R)hv)^{2/n}$ against $h\nu$, corresponded to the x-axis intersection point of the linear fit of the Tauc plot. Note that PCN samples were treated as the semiconductors with the indirect transition band gaps.

Ultraviolet photoelectron spectroscopy (UPS) was further used to determine the ionization potential (Figure S23) in order to measure the valence band energy (E_{VB})^[9]. According to the linear intersection method, the E_{VB} of CN was calculated to be -5.99 eV (vs. vacuum)

$$-E_{VB} = hv + E_{Fermi} - E_{Cutoff}$$

Where hv is 21.22 eV, the excitation energy of the He I Source Gun, E_{Fermi} is -0.64 eV, and E_{Cutoff} is 14.59 eV.

Then the E_{VB} of CN vs. RHE, was converted to be 1.55 V, on the basis of the relationship between the vacuum energy (E_{vacuum}) and the RHE potential (E_{RHE}),

$$E_{vacuum} = -E_{RHE} - 4.44 \text{ eV}$$

Combined the VB maximum difference between the CN and other PCN based samples from the VB-XPS results, the E_{VB} of the other PCN based samples could be collected^[10]. The together with the bandgap values from the DRS spectra, the band positions of PCN based samples could be obtained.

3. Figures and discussions

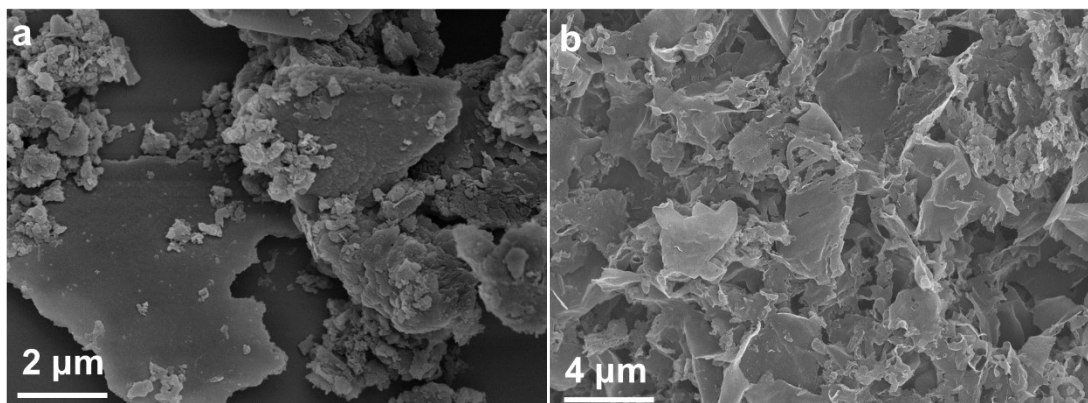


Figure S1. SEM images of (a) CN and (b) HCN. CN is synthesized by directly calcination of DCDA, HCN is synthesized via two steps: hydrothermal pretreatment with DCDA, then the obtained intermediate was calcinated.

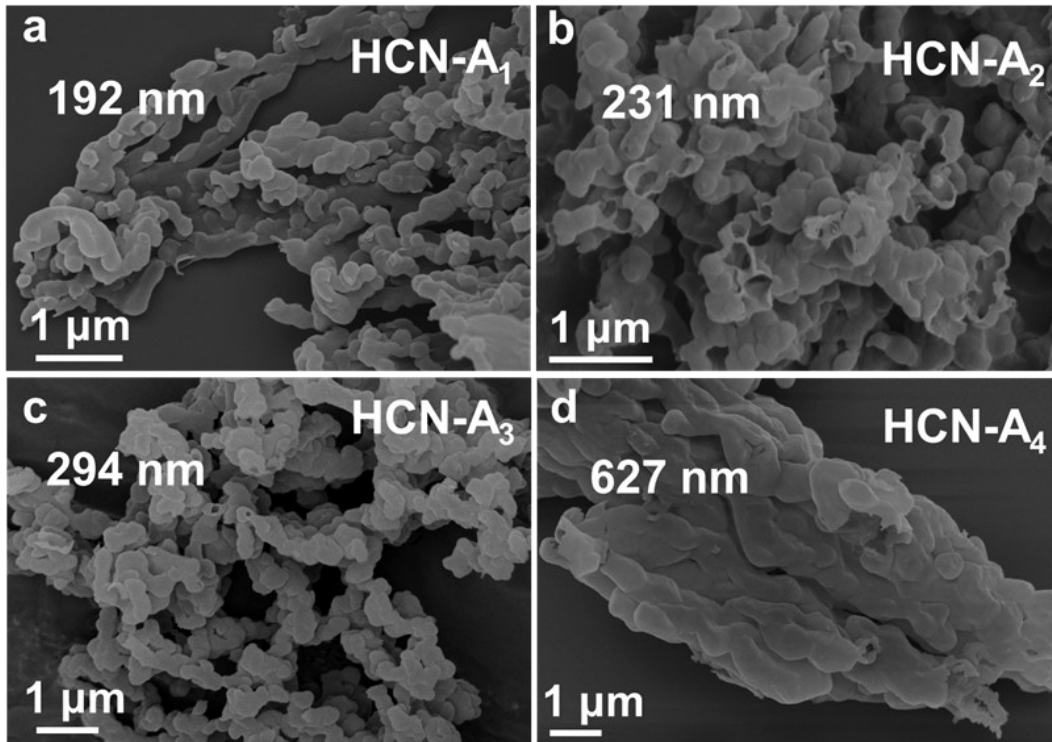


Figure S2. SEM images of (a) HCN-A₁, (b) HCN-A₂, (c) HCN-A₃, and (d) HCN-A₄.

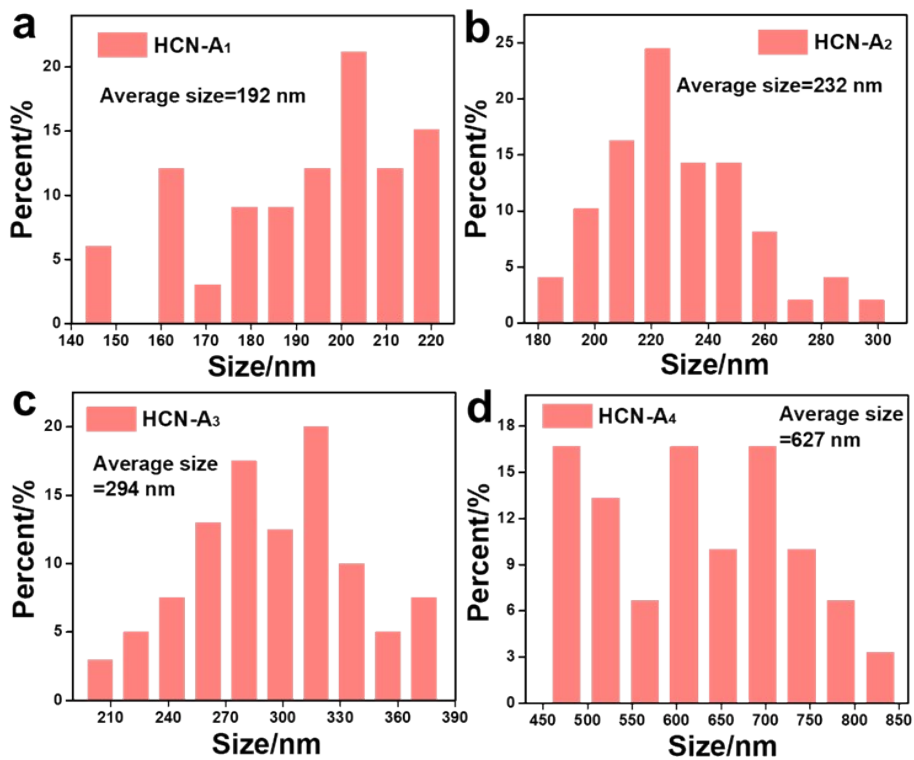


Figure S3. The corresponding size distribution measured from the SEM images in **Figure S2** of (a) HCN-A₁, (b) HCN-A₂, (c) HCN-A₃, and (d) HCN-A₄.

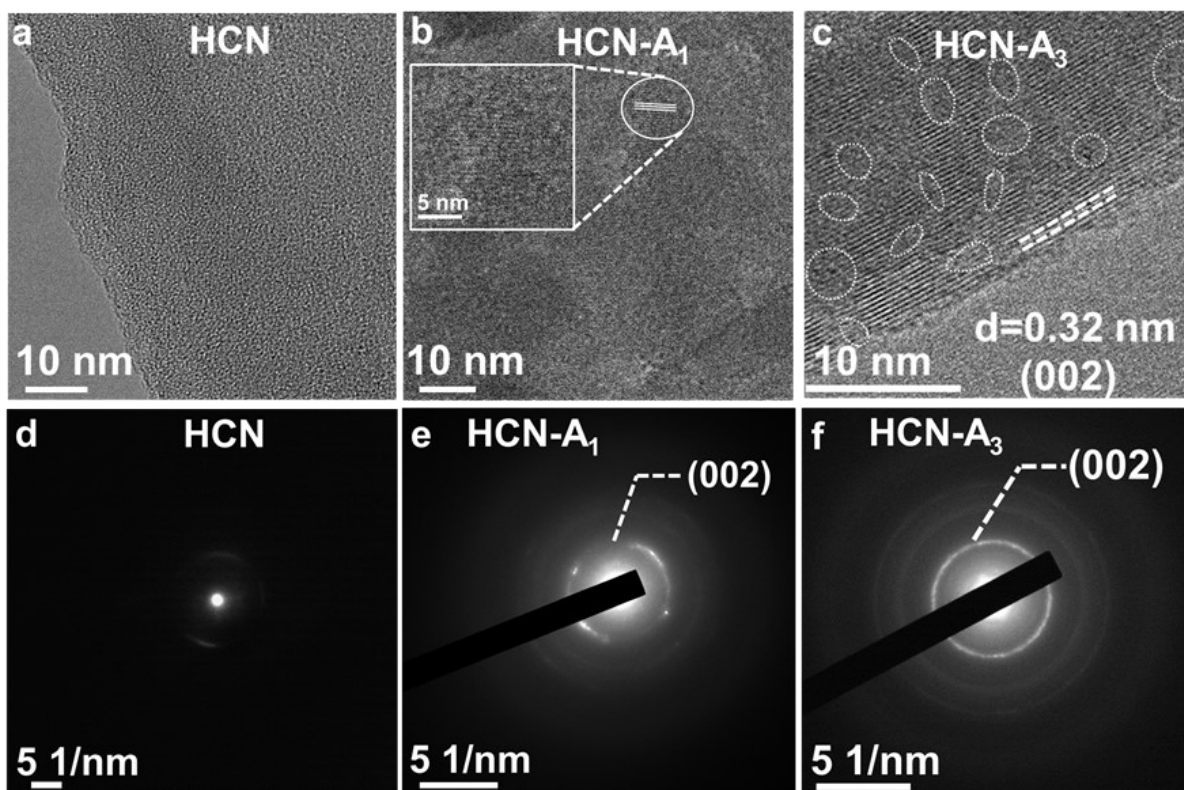


Figure S4. HR-TEM of (a) HCN, (b) HCN-A₁ and (c) HCN-A₃. The correspondingly selected area electron diffraction (SAED) of (d) HCN, (e) HCN-A₁ and (f) HCN-A₃.

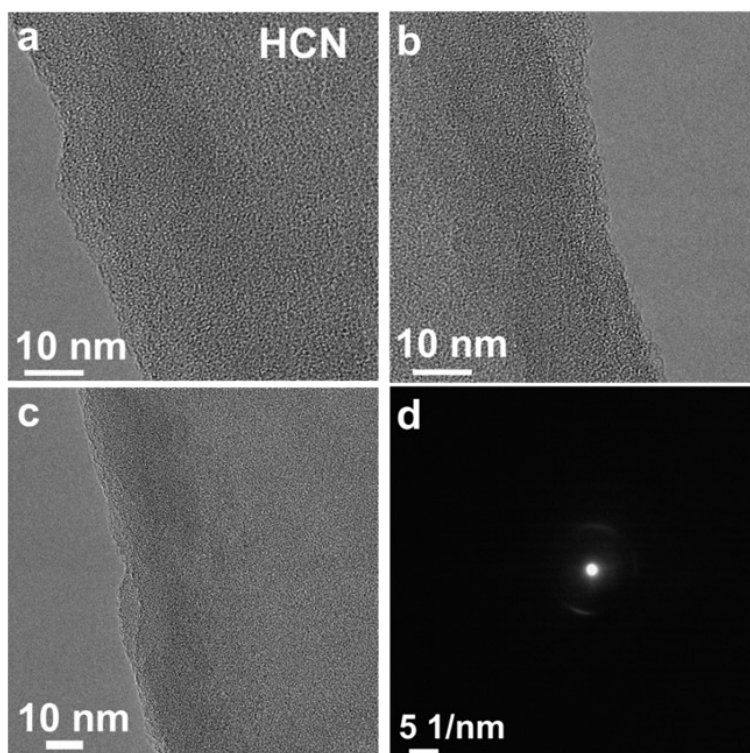


Figure S5. HR-TEM of (a-c) HCN and (d) the correspondingly selected area electron diffraction (SAED) image.

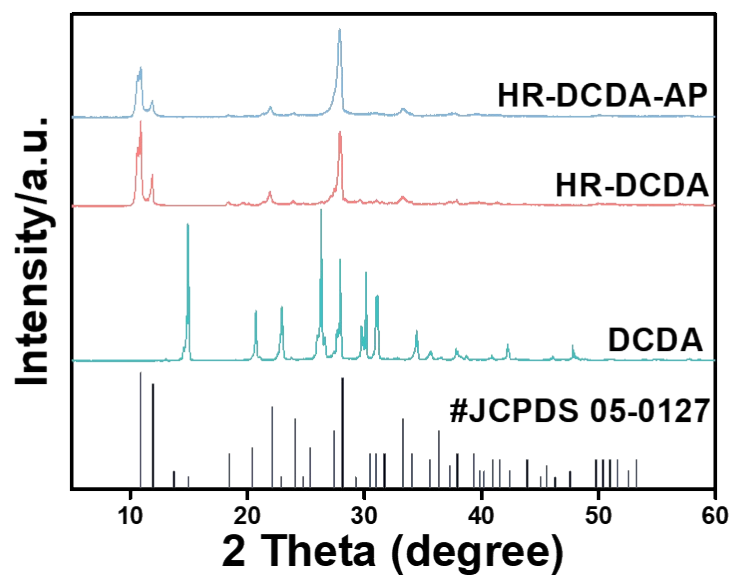


Figure S6. XRD patterns of the precursor dicyandiamide (DCDA), the intermediate solids after the hydrothermal pretreatment of dicyandiamide (HR-DCDA) and the modified intermediate after the addition of amino-2-propanol (AP) during hydrothermal process of dicyandiamide (HR-DCDA-AP). The #JCPDS 05-0127 is the XRD standard card of melamine-cyanurate acid complex.

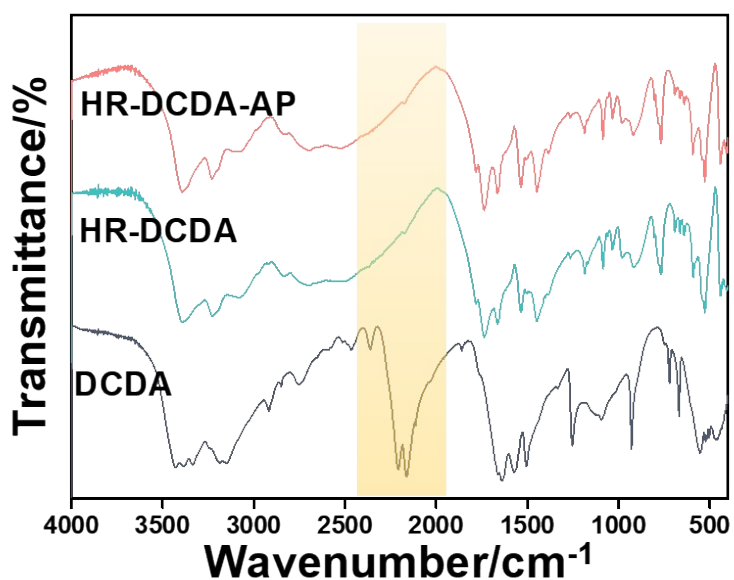


Figure S7. FTIR spectra of DCDA, HR-DCDA, and HR-DCDA-AP.

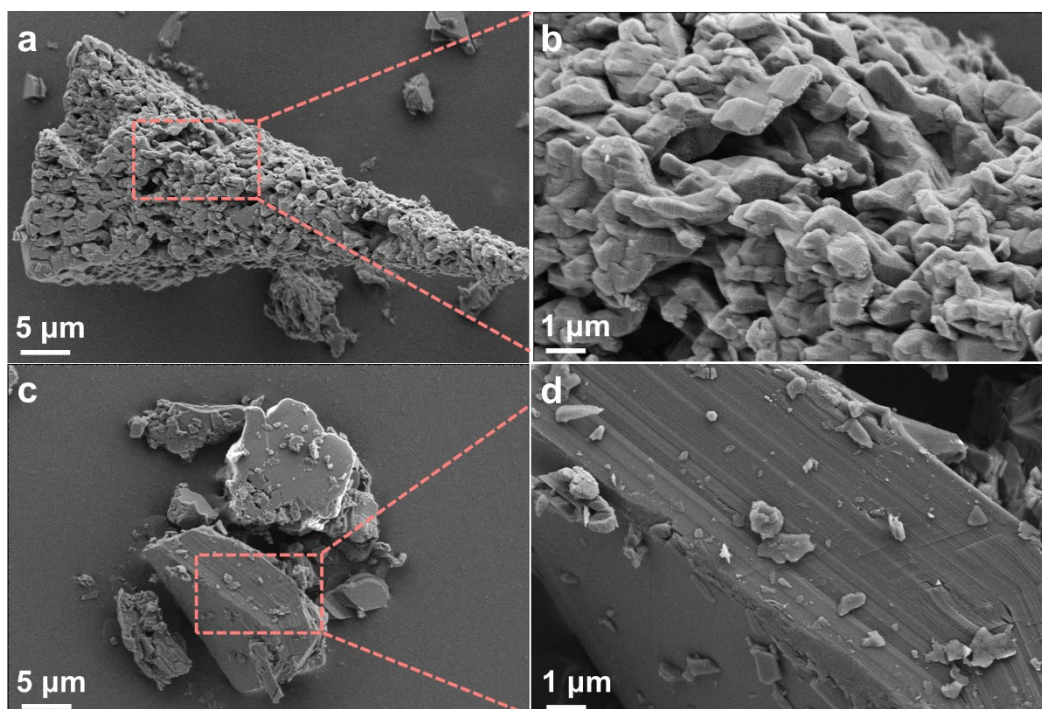


Figure S8. SEM images of the obtained intermediate (a, b) HR-DCDA-AP and (c, d) HR-DCDA after hydrothermal pretreatment of DCDA. Image (b) and (d) are the enlarged pictures from the close-up of area marked in the square of (a) and (c), respectively.

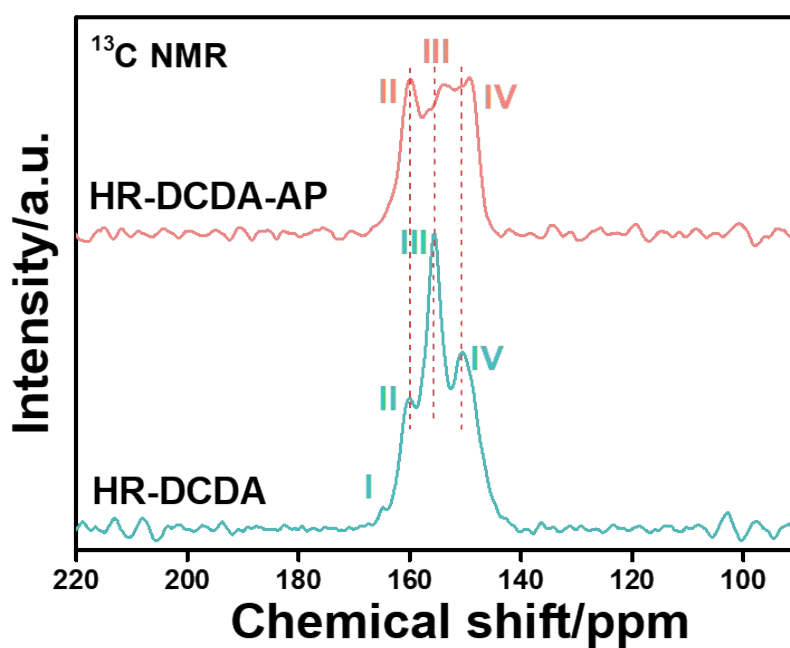


Figure S9. Solids state ¹³C NMR spectra of HR-DCDA and HR-DCDA-AP samples.

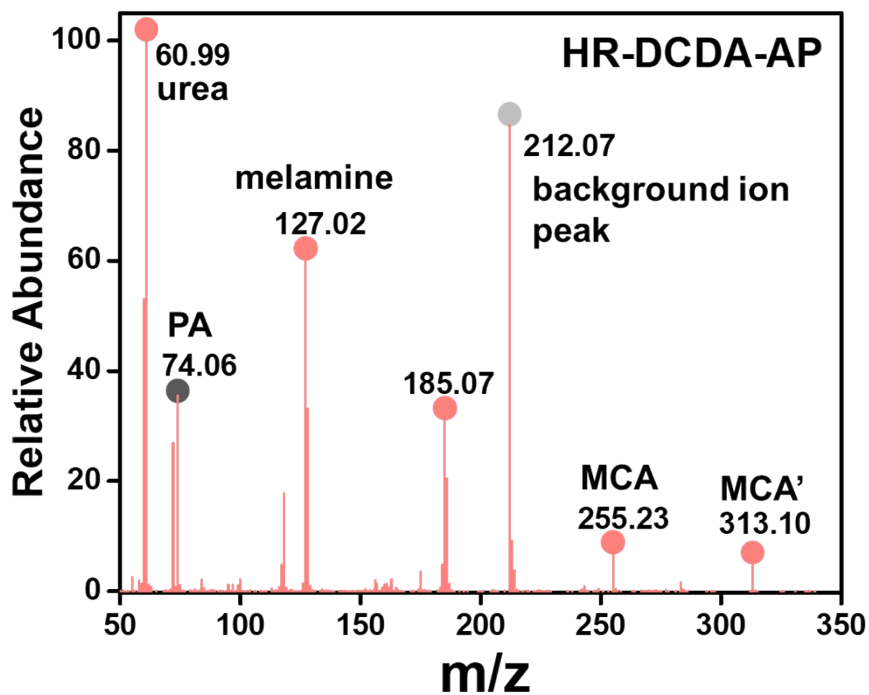


Figure S10. Mass spectrometry (MS) analysis results of the intermediate HR-DCDA-AP by hydrothermal treatment of dicyandiamide (DCDA) and amino-2-propanol (AP).

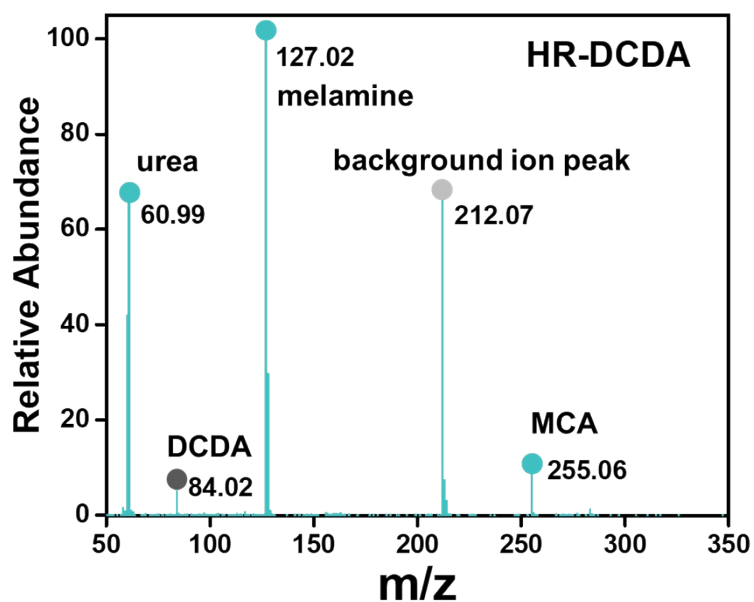


Figure S11. Mass spectrometry (MS) analysis results of the intermediate HR-DCDA by hydrothermal treatment of dicyandiamide (DCDA).

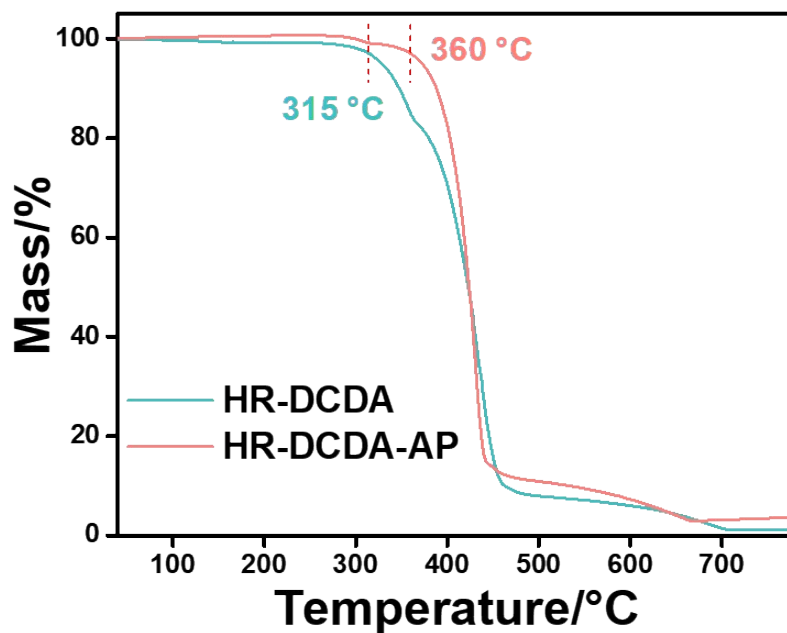


Figure S12. Thermogravimetric (TG) curve of HR-DCDA and HR-DCDA-AP samples.

Additional discussions:

To clarify the role of AP during the HCN-A catalyst preparation process, X-ray diffraction (XRD) experiments (Figure S6) of the precursor well matches the melamine-cyanurate acid (MCA) complex (#PDF 05-0127), further confirmed by the Fourier-transform infrared spectroscopy (FTIR) spectra (Figure S7)^[11]. Scanning electron microscopy (SEM) images present the precursor composed of elliptic stacked aggregates (Figure S8). Meanwhile, the intermolecular hydrogen bonding was investigated by ¹³C solid-state NMR (Figure S9), the addition of AP leads to shift of 2.5 ppm toward the high field relative to the peak III and IV in which these two signals are ascribed to the chemical shift of carbon atoms from cyanuric acid in the MCA system^[12]. Notably, the presence of chemical shifts indicates the chemical non-equivalence of the alteration environment of hydrogen bonded carbon sites. The high field shift after the AP addition means the intensive shielding effect of H-bonding interaction and decrease in bond length, further signifying the increase electron cloud density surrounding the carbon atom on the H-bonding and improving the degree of crystallinity^[13]. Meanwhile, it is worth mentioning

that the ESI-MS spectrum manifests molecular weight of the AP modified precursor is increased from 255 to 313 and a new mass fragment at $m/z=185$ is generated (Figure S10 and Figure S11), suggesting the alkylamine ligands in AP preferentially coordinated with the cyanuric acid units^[14], thus strengthening the H-bonding interaction and forming the crystallized matrices. And the thermogravimetric (TG) curve of AP modified precursor presents the higher thermal decomposition temperature from 315 to 360 °C (Figure S12), implying the stronger thermal stability. Collectively, the addition of AP during the hydrothermal process experiences the higher polymerization degree, the intensive H-bonding interaction, and traitor the morphology of the melamine-cyanurate acid complex.

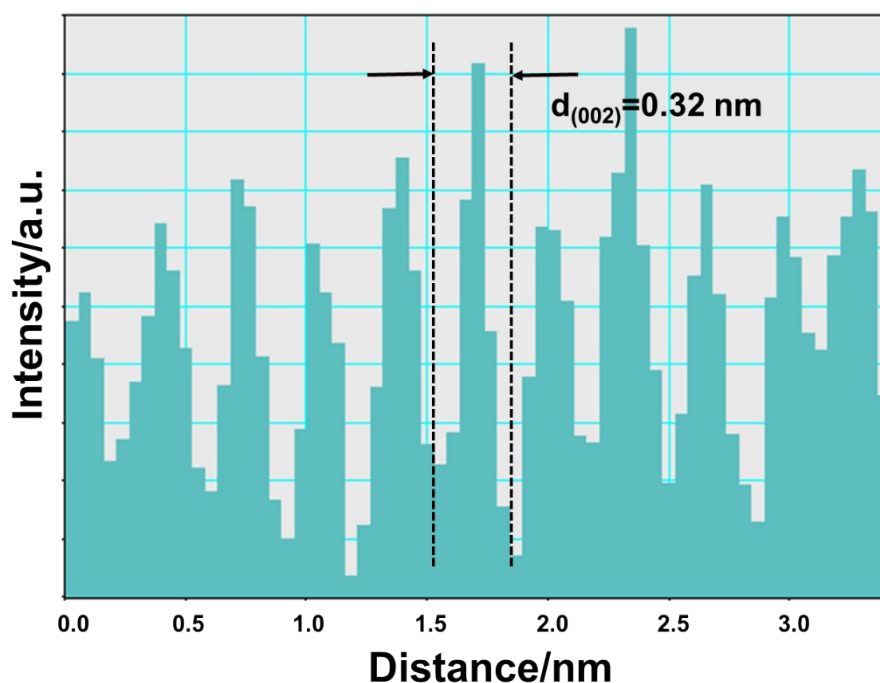


Figure S13. Line-scanning intensity profile obtained from Figure 1f.

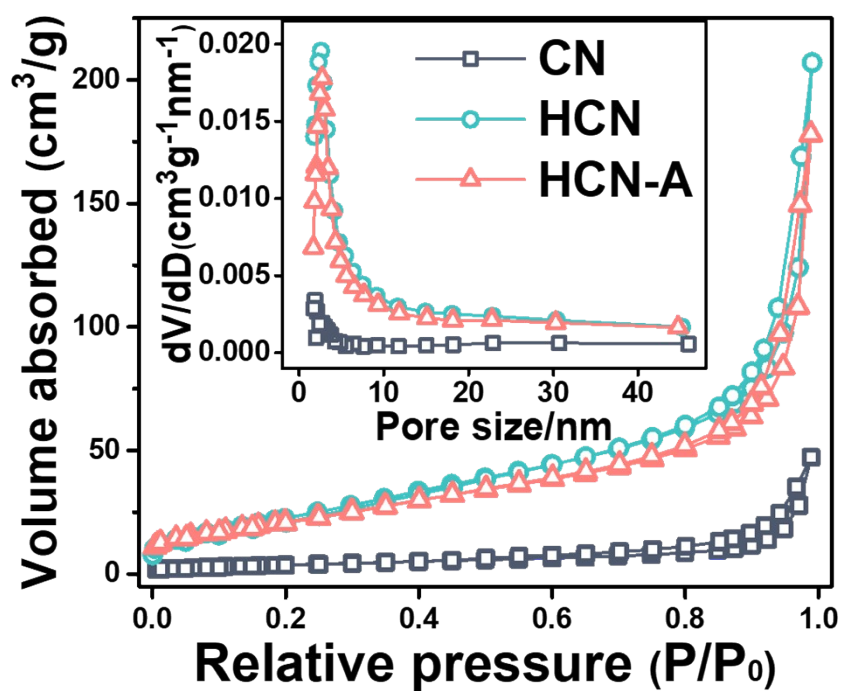


Figure S14. The specific surface area of the resultant CN, HCN, HCN-A. Inset is the pore distribution plots.

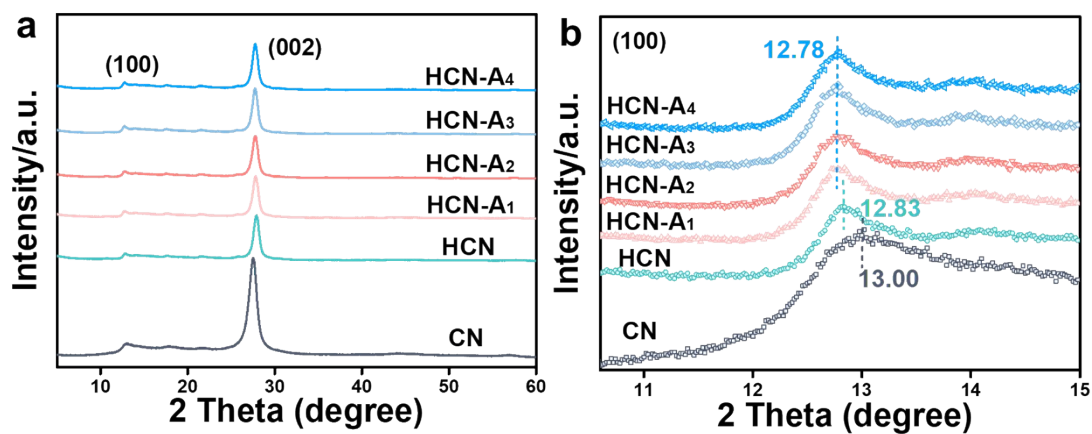


Figure S15. (a) XRD patterns and (b) the enlarged (100) plane of CN, HCN, HCN-A₁, HCN-A₂, HCN-A₃, and HCN-A₄.

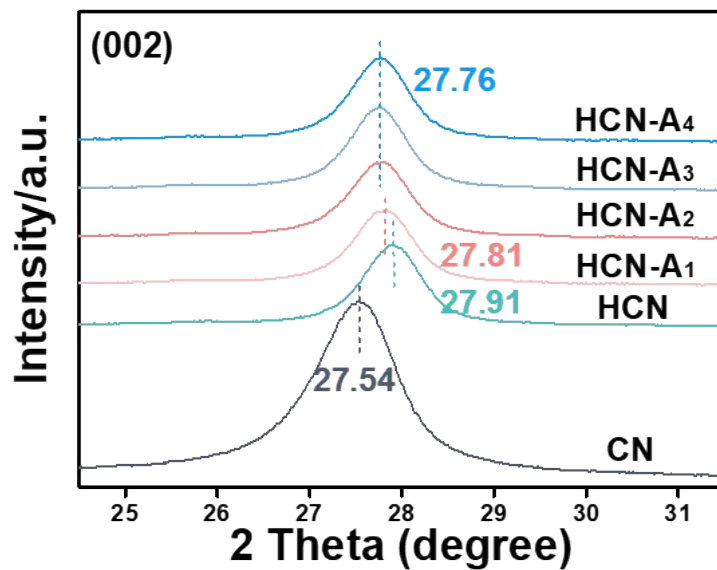


Figure S16. The enlarged (002) plane of CN, HCN, HCN-A₁, HCN-A₂, HCN-A₃, and HCN-A₄.

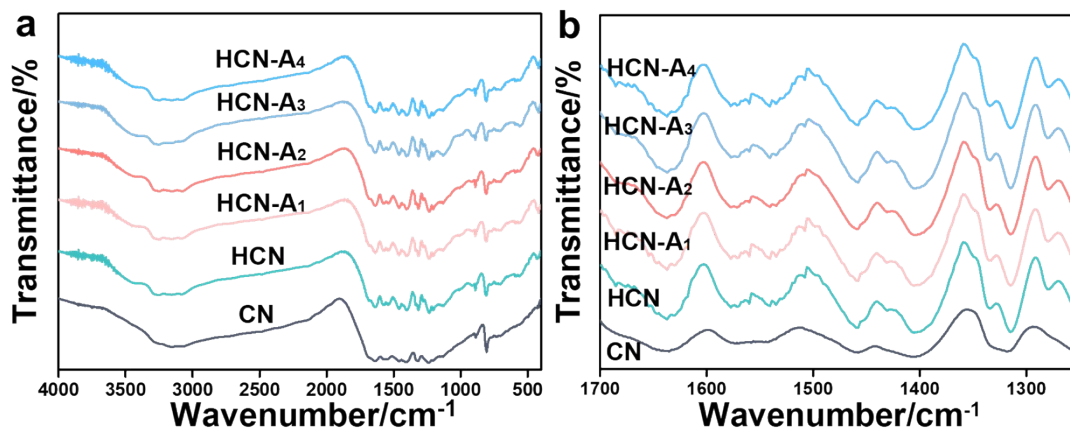


Figure S17. FTIR spectra of CN, HCN, HCN-A₁, HCN-A₂, HCN-A₃, and HCN-A₄.

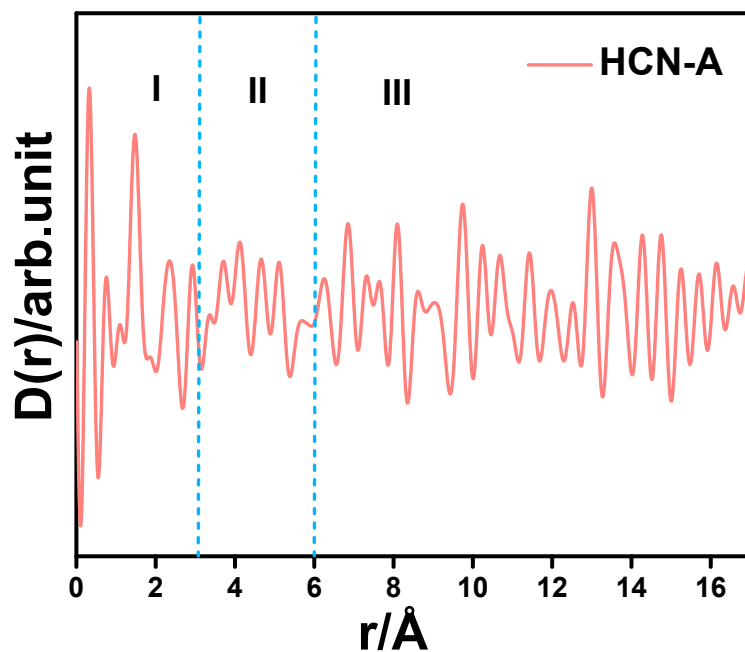


Figure S18. Differential correlation function of $D(r)$ of HCN-A after Fourier transform with the PDFgui refinement.

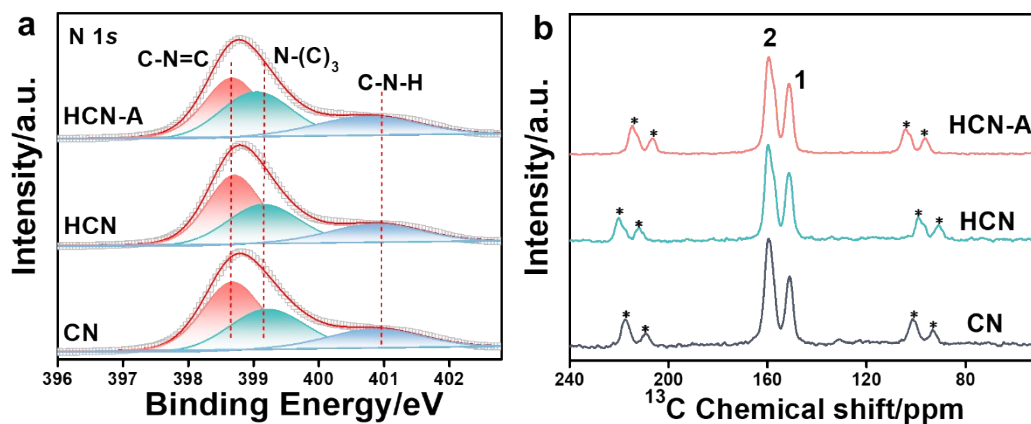


Figure S19. (a) XPS high resolution spectra of N 1s and (b) Solid ^{13}C NMR spectra in CN, HCN, and HCN-A, * represents the spinning sidebands in the ^{13}C NMR spectra.

Additional discussions:

The high-resolution X-ray photoelectron spectroscopy (XPS) N 1s spectrum in HCN-A was deconvoluted into three types of N levels in the asymmetric peaks (Figure S17); the peaks at the

binding energy of 398.6, 399.0 and 400.8 eV are assigned to pyridinic (C-N=C), pyrrolic (N-(C)₃) and amino (C-N-H) nitrogen^[11]. While, the carbon contents and N-(C)₃/ C-N=C ratios of HCN-A are listed in Table S2-S4. And we also provide the solid-state ¹³C MAS NMR spectra in Figure S19b, all of the samples presented two characteristic peaks located at the same position of 151.2 and 159.9 ppm, assigned to the C-(N)₃ and NH₂-C(N)₂ in tri-s-triazine motifs, respectively. It is not observed the generation of any new peaks in HCN-A, manifesting the addition of AP (amino-2-propanol) may not alter the chemical structure of the carbon nitride matrix network.

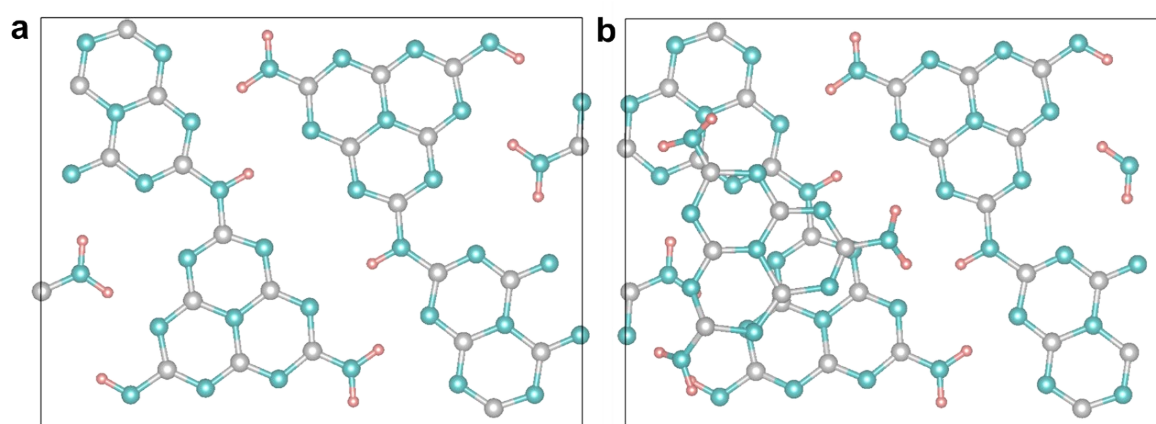


Figure S20. Calculated models of the structure cell, (a) HCN and (b) HCN-A. The grey, cyan, and teal red color sphere denote the carbon, nitride, and hydrogen atom respectively.

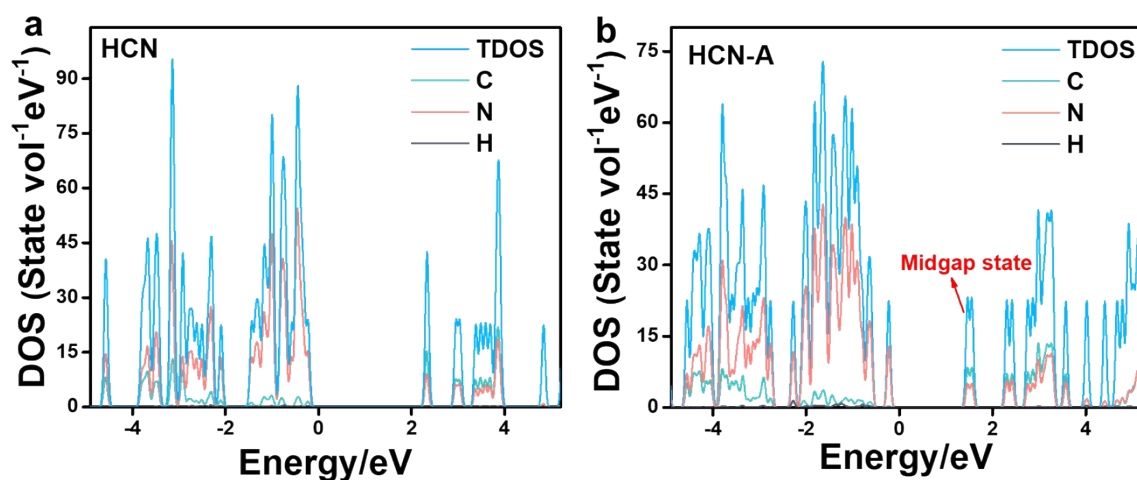


Figure S21. Total and partial density of states over (a) HCN and (b) HCN-A.

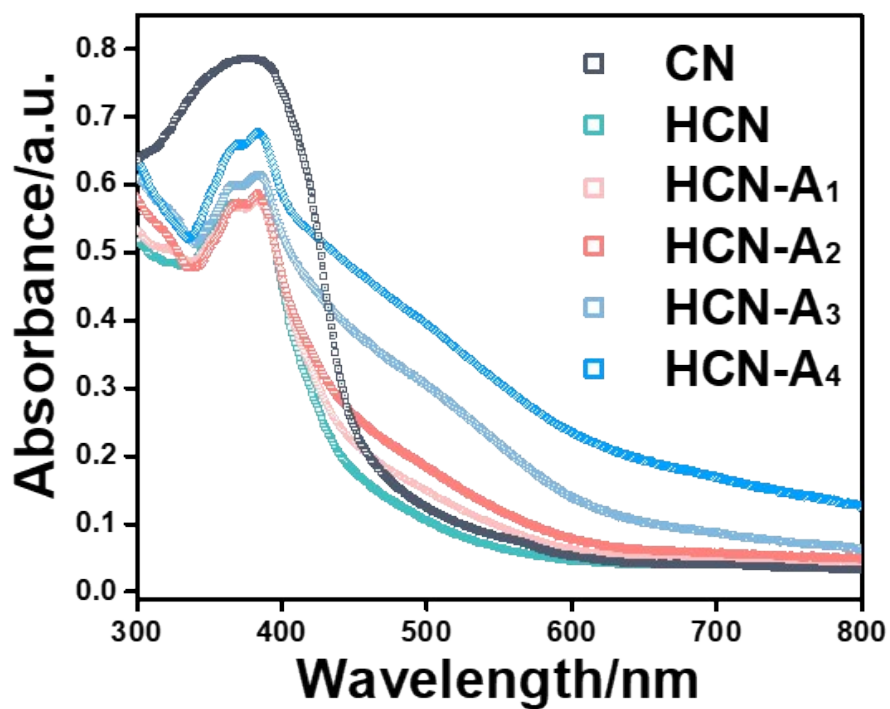


Figure S22. Diffuse reflectance UV-Vis (DRS) spectra of CN, HCN, HCN-A₁, HCN-A₂, HCN-A₃, and HCN-A₄.

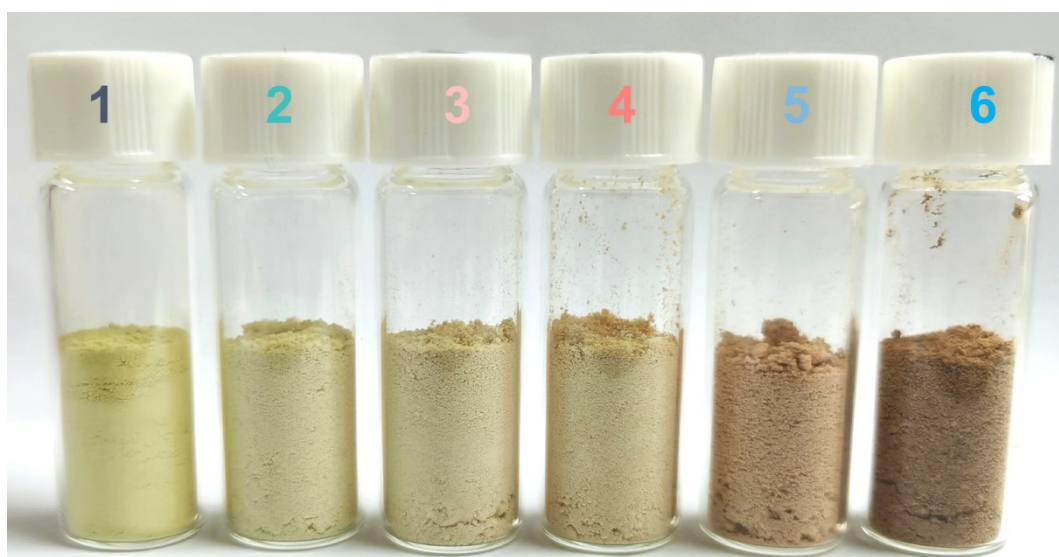


Figure S23. Digital picture of CN (1), HCN (2), HCN-A₁ (3), HCN-A₂ (4), HCN-A₃ (5), and HCN-A₄ (6).

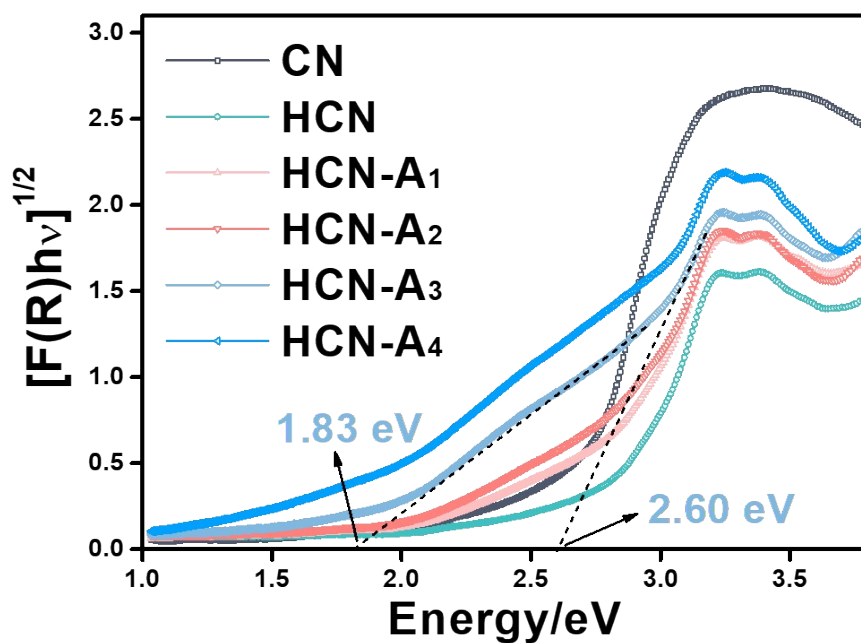


Figure S24. The calculated band gap of catalyst samples converted using the Kubelka-Munk function from DRS spectra.

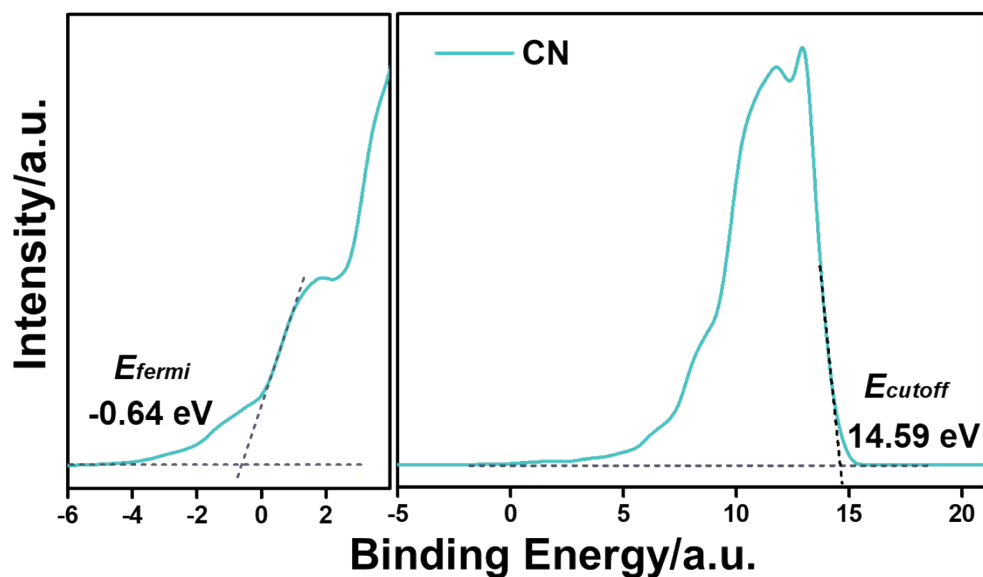


Figure S25. UPS spectrum of CN. UPS was used to determine the ionization potential, which is equivalent to the valence band energy (E_{VB}). The calculated process seen in the Supplementary Note 2.

Additional discussions:

According to the linear intersection method, the E_{VB} of CN was calculated to be -5.99 eV (vs. vacuum)

$$-E_{VB} = hv + E_{Fermi} - E_{Cutoff}$$

Where hv is 21.22 eV, the excitation energy of the He I Source Gun, E_{Fermi} is -0.64 eV, and E_{Cutoff} is 14.59 eV.

Then the E_{VB} of CN vs. RHE, was converted to be 1.55 V, on the basis of the relationship between the vacuum energy (E_{vacuum}) and the RHE potential (E_{RHE}),

$$E_{vacuum} = -E_{RHE} - 4.44 \text{ eV}$$

VB maximum difference between CN, and HCN-A determined from VB-XPS spectra (Figure S24), one can get E_{VB} of HCN-A, vs. RHE. Combined with the bandgap values calculated from UV-vis diffuse reflectance spectra (DRS), the band positions of CN, HCN and HCN-A could be then achieved.

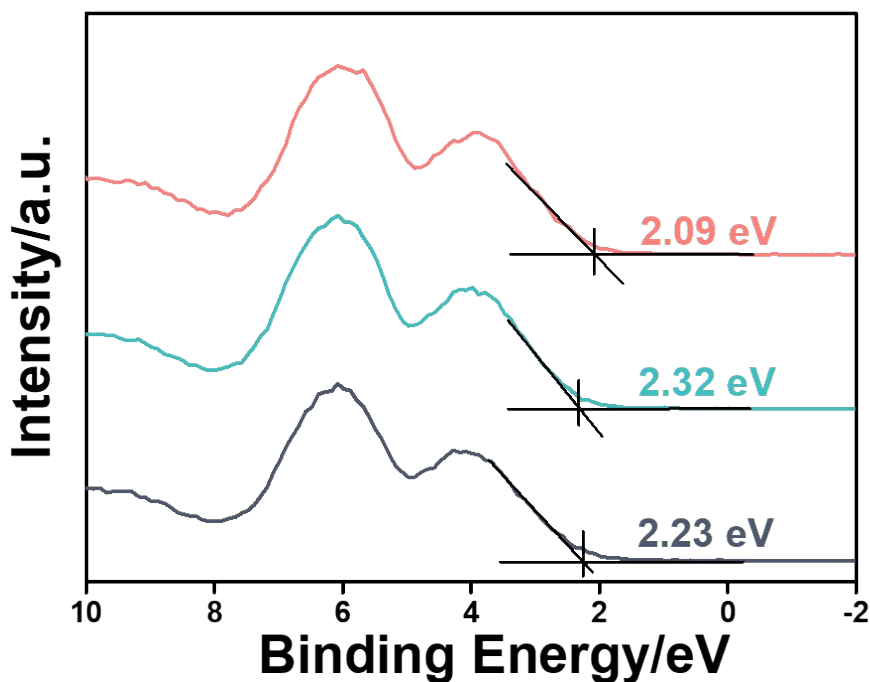


Figure S26. Valence band (VB)-XPS spectra of CN, HCN, and HCN-A.

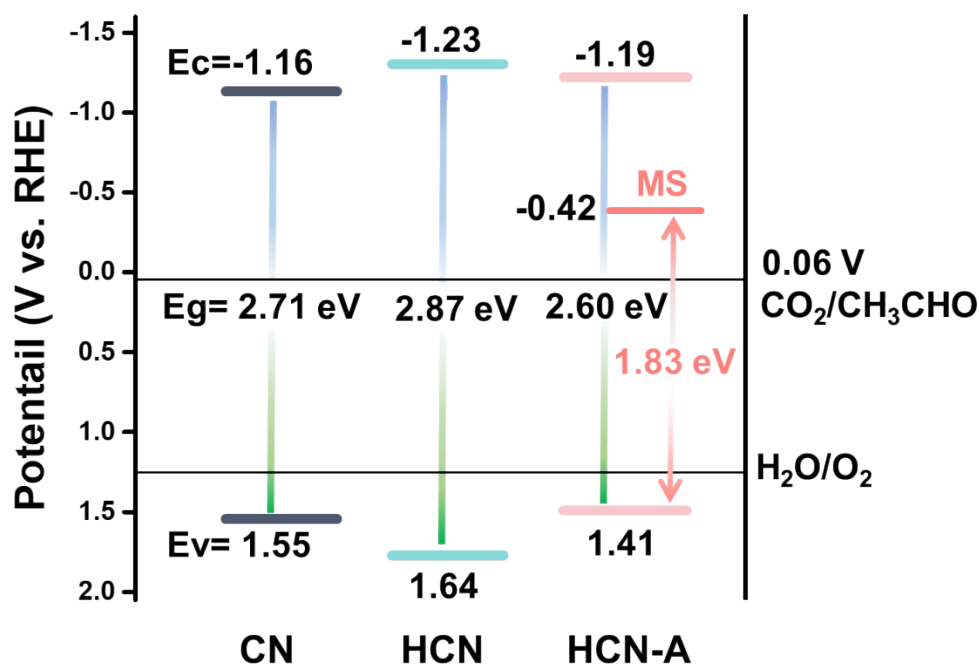


Figure S27. Band structure alignments for CN, HCN, and HCN-A catalyst samples.

Additional discussions:

The UV-vis diffuse reflectance spectroscopy (DRS) in Figure S22 depicts that HCN-A exhibits the intensive absorption along the 450-800 nm and a red-shift of the intrinsic absorption edge of carbon nitride. And another step-like absorption tail extending to 700-900 nm appears in the HCN-A₃ and HCN-A₄, indicating that dyadic heterostructures-related midgap states (MS) are generated in the band gap of HCN-A. This was visually evidenced by the digital picture of these samples from the color variation (Figures S23). The enhanced absorption capability in HCN-A contributes towards the strengthened activity, the prerequisite for successfully visible-light-driven CO₂ conversion. As determined by the Kubelka–Munk function (Supplementary Note 2), the intrinsic bandgaps of HCN-A is 2.59 eV (Figures S24), smaller than CN (2.71 eV) and HCN (2.87 eV). And a bandgap of 1.85 eV, corresponding to the electronic transition between the valence band (VB) and MS, was measured for HCN-A₃. As revealed by the UPS (Figures S25) and VB XPS spectra (Figures S26), the VB maximum is reduced from 1.64 eV for HCN to 1.41 eV for HCN-A as with the enhanced concentration of AP addition.

Therefore, the band alignment position of the synthesized samples could be proposed in Figures S27 and the conduction band (CB) is negative enough for efficient CH_3CHO generation (0.06 V vs. RHE).

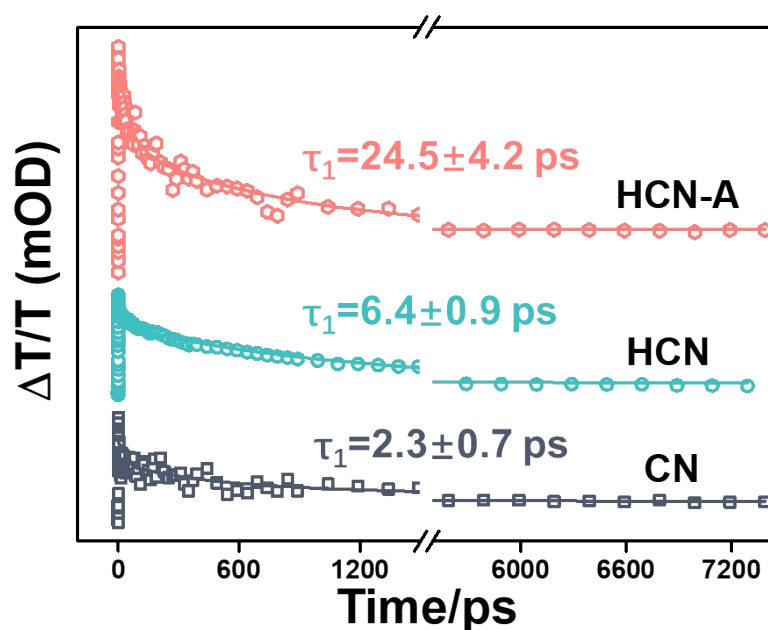


Figure S28. Carrier dynamics of CN, HCN and HCN-A after subtracting the ground state bleach signal after excitation at zero delay time.

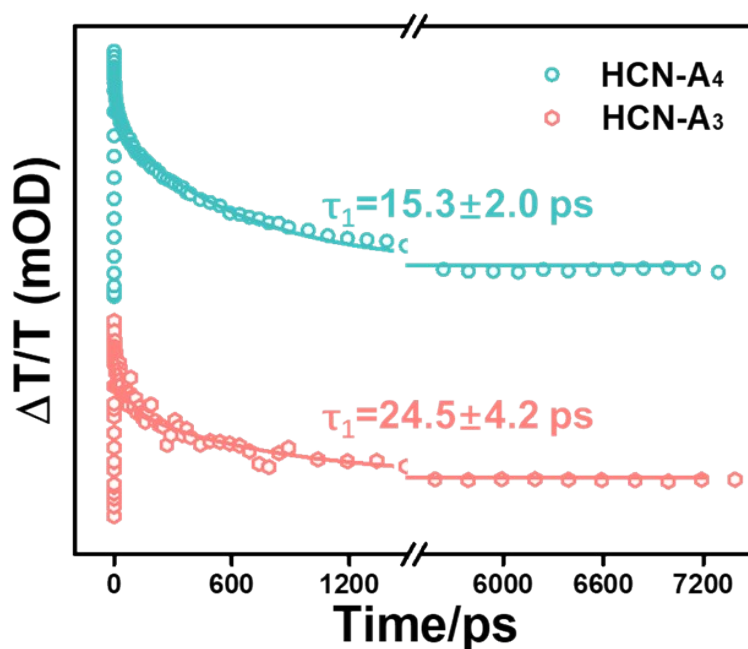


Figure S29. Carrier dynamics of HCN-A₃ and HCN-A₄ after subtracting the ground state bleach signal after excitation at zero delay time.

Additional discussions:

femtosecond transient absorption measurements (fs-TA) was resorted to investigate the electronic excited state kinetic after light illumination (Figure S28). The short relaxation lifetime was routinely employed as an indicator to evaluate charge separation efficiency (i.e. the longer the relaxation, the higher the efficiency). The longest relaxation time of 24.5 ± 4.2 ps observed in HCN-A (HCN-A₃) than that of HCN (6.4 ± 0.9 ps) and CN (2.3 ± 0.7 ps) echoes well to the most predominant CH₃CHO production rate of HCN-A, indicating that the optimized dyadic HCN-A sample achieves the efficient charge separation^[15]. What's more, as shown in Figure S29, HCN-A₃ shows the longer charge carrier lifetime of 24.5 ± 4.2 ps, which is significantly higher than HCN-A₄ (15.3 ± 2.0 ps). This indicates that the well-defined hollow sphere structure of HCN-A₃ benefits the efficient charge separation than the aggregated structure in HCN-A₄. Therefore, HCN-A₄ possesses the lower photocatalytic performance than HCN-A₃.

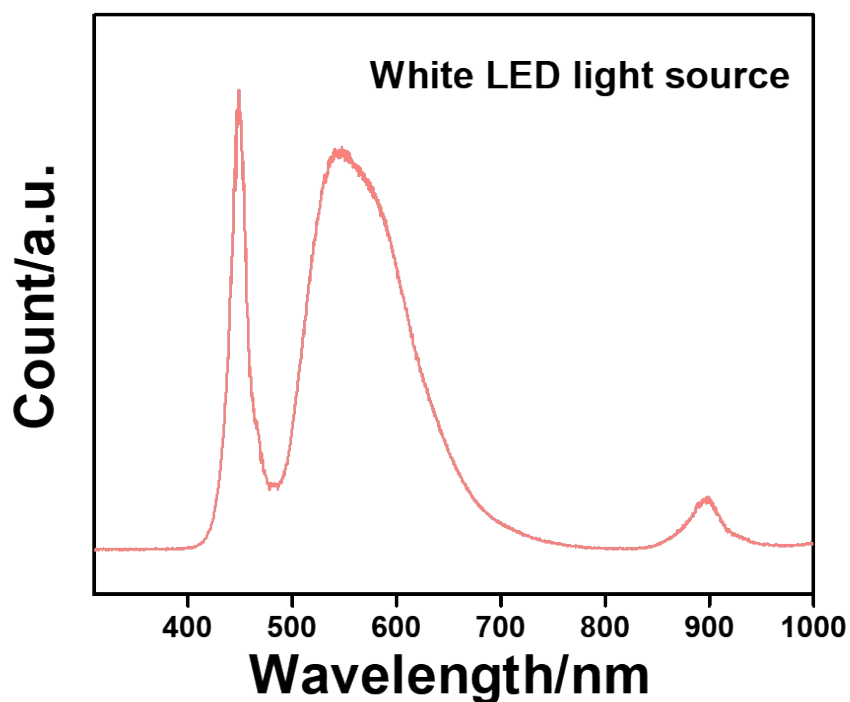


Figure S30. The excited wavelength of the using white LED light source.

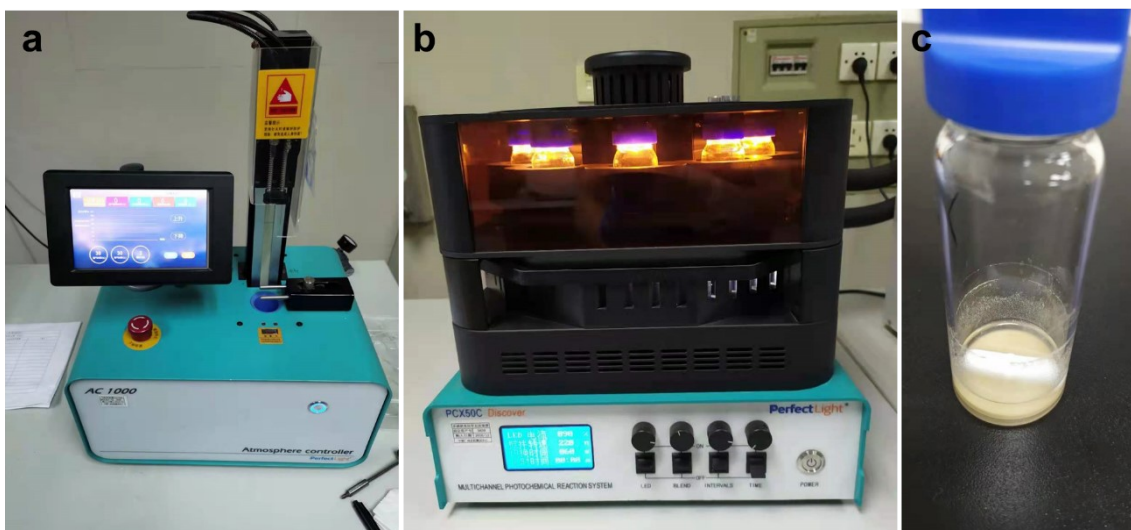


Figure S31. (a) The atmosphere controller used to degas the air and filled into the high pure CO₂ gas into the reactor. (b) The photocatalytic reaction setup. (c) Photoreactor.

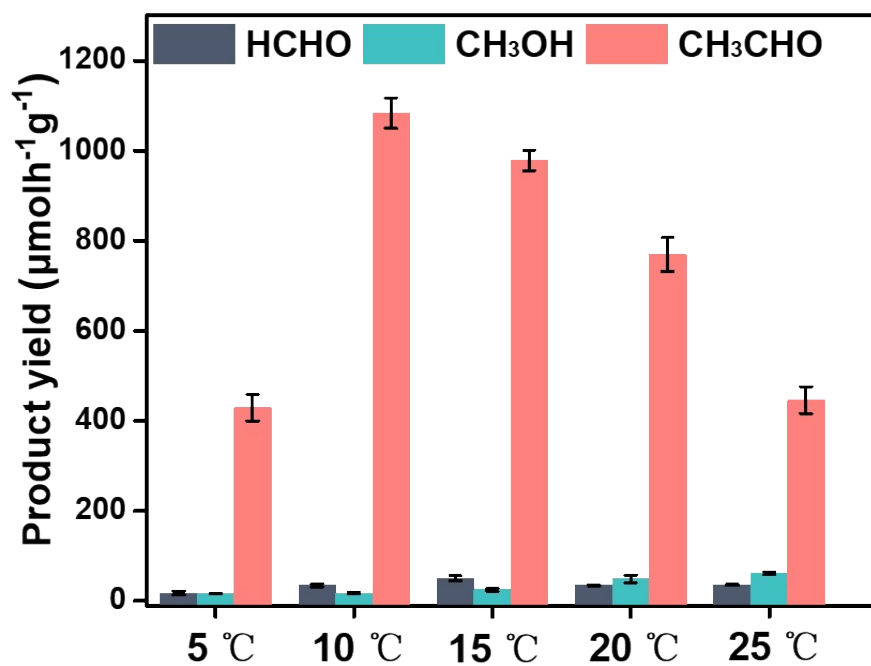


Figure S32. The average generation rate of CO₂ reduction products by using HCN-A as the catalyst with 3 mL solvent.

Additional discussions:

The photocatalytic CO₂ reduction was investigated using the Multi-channel photochemical reaction system equipped with a 5 W white LED lamp (light density =100 mWcm⁻²) at the temperature of 10 °C and ambient pressure (the excited wavelength of light source shown in Figure S30, photographs of the devices used in the measurement shown in Figure S31). The reaction suspension contains the carbon nitride catalyst, the mixture of acetonitrile, water and triethanolamine (TEOA) solution, and without metal cocatalyst involved. The optimized temperature of 10 °C is according to the performance activity of HCN-A at a series of different temperature (Figure S32). It is clearly observed the reaction temperature at 10 °C could gain the best photocatalytic performance, when using the routinely exploited 25 °C, the performance is intensively retarded. The evolved CH₃CHO was quantified using the external standard method (Figure S33).

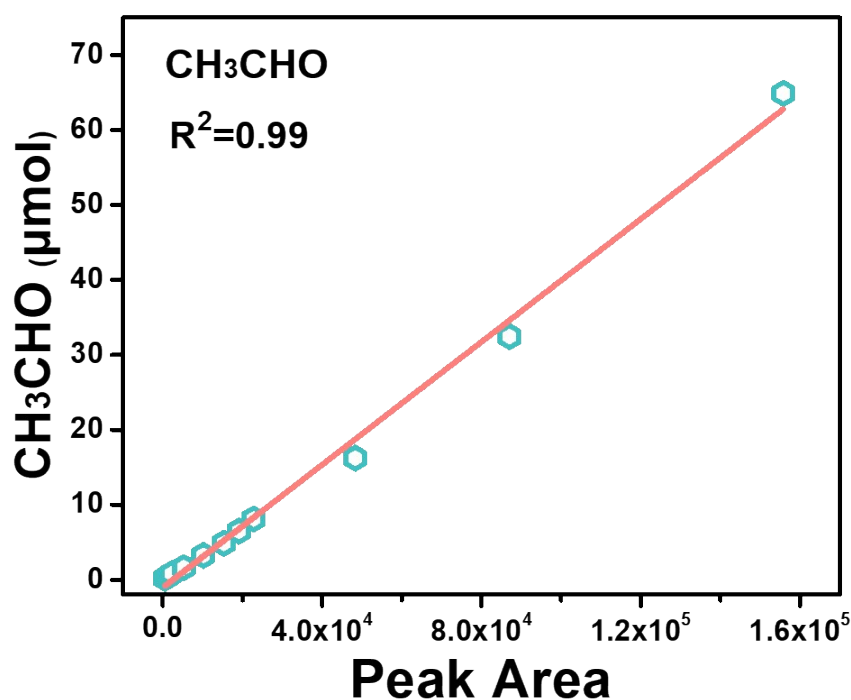


Figure S33. Calibration curves of GC for the quantification of CH₃CHO.

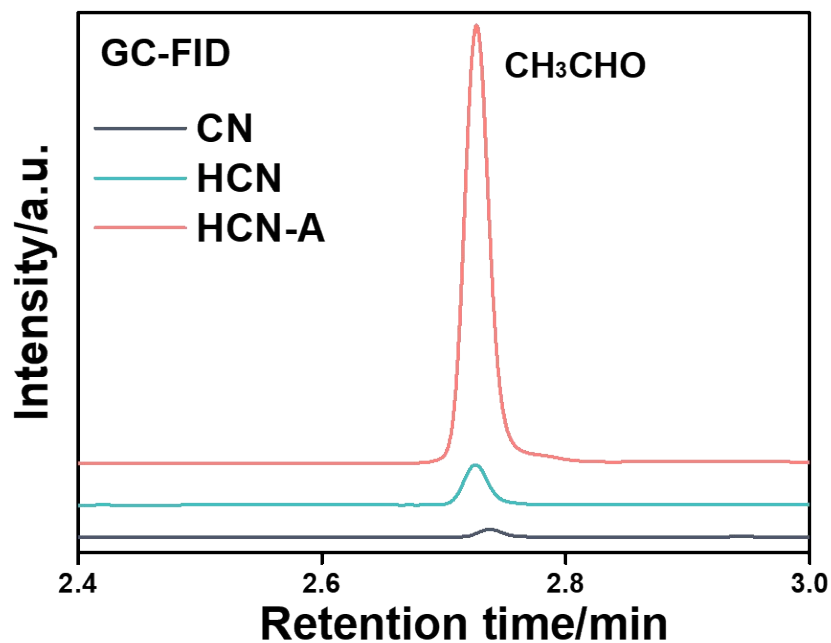


Figure S34. GC/FID signals for CH₃CHO over the CN, HCN, and HCN-A catalysts.

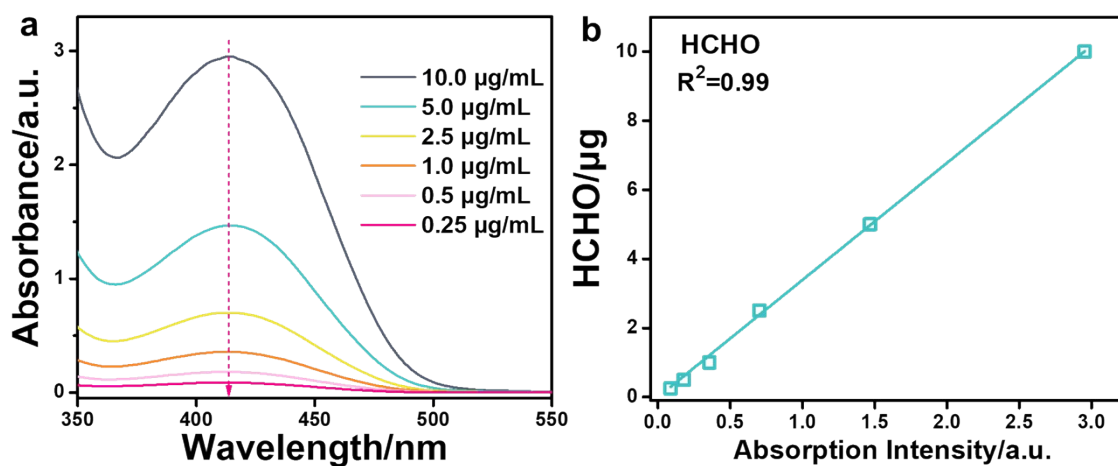


Figure S35. Calibration curves for the quantification of HCHO by using acetylacetone colour-development method.

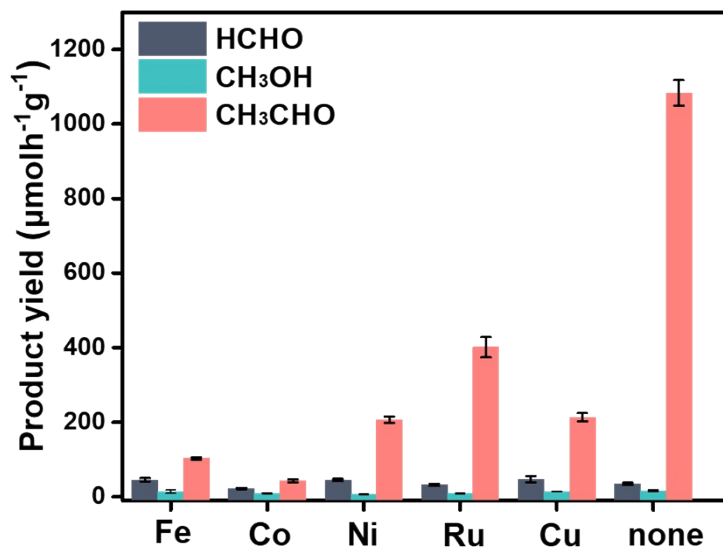


Figure S36. The average generation rate of CO₂ reduction liquid products by using HCN-A as the catalyst with the 3 mL solvent at the temperature of 10 °C, and the 1 μmol of metal complex was added or not any metal species was involved. Note that the metal complex is constituted with the metal chloride with appropriate amount of dipyrindine, such as the [Co(bpy)₃]²⁺ (bpy=2,2'-bipyridine) or [Ru(bpy)₃]²⁺.

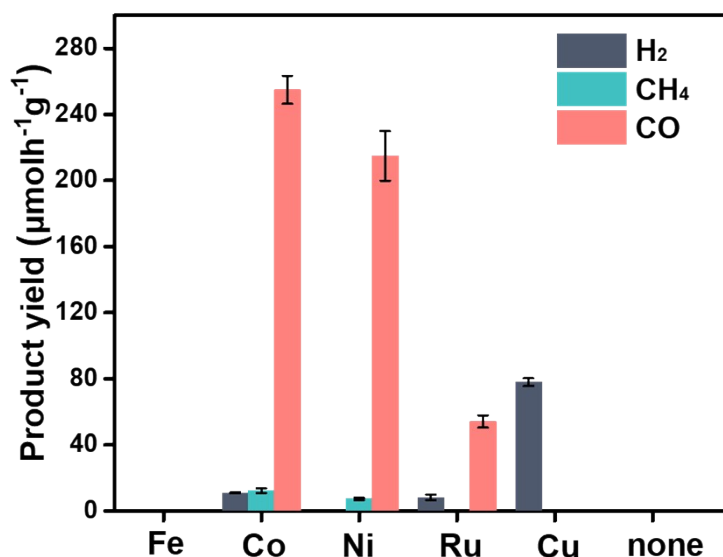


Figure S37. The average generation rate of CO₂ reduction gaseous products by using HCN-A as the catalyst with the 3 mL solvent at the temperature of 10 °C, and the 1 μmol of metal complex was added or not any metal species involved.

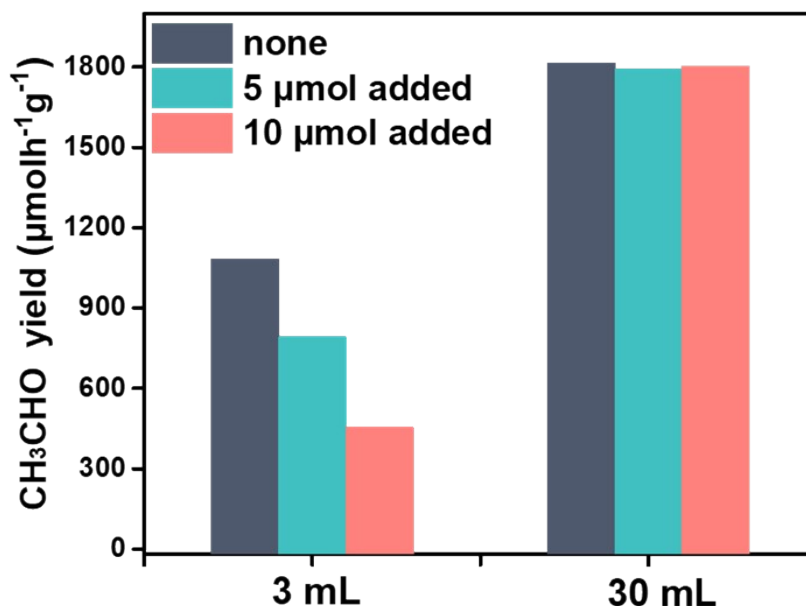


Figure S38. The CH₃CHO product yield under the control condition of 0, 5 and 10 μmol CH₃CHO solvent addition in 3 or 30 mL reaction systems. The product yield of CH₃CHO was calculated by subtracting the CH₃CHO addition (5 or 10 μmol) from the total detected CH₃CHO after photocatalytic reaction.

Additional discussions:

We added 5 or 10 μmol CH₃CHO solvent in our applied 3 mL or 30 mL reaction solvent using HCN-A as catalyst before illumination. After 2 hours, the liquid sample was analyzed by GC-FID. The corresponding product yield of CH₃CHO was calculated by the total detected CH₃CHO value minus the added 5 or 10 μmol CH₃CHO. If we assumed the formed CH₃CHO would not retard the following formed product, the generated CH₃CHO yield may remain unchanged. However, as shown in Figure R3, the CH₃CHO product yield is obviously retarded after the extra addition of CH₃CHO solvent in 3 mL reaction solvent, but the CH₃CHO addition would not decrease the activity in 30 mL reaction solvent. As such, The result indicates the increase in CH₃CHO product yield in 30 mL may due to dilution of the initially formed CH₃CHO. In this case, the increase in CH₃CHO product yield is due to dilution of the initially formed CH₃CHO limits its product accumulation and the reaction equilibrium shift.

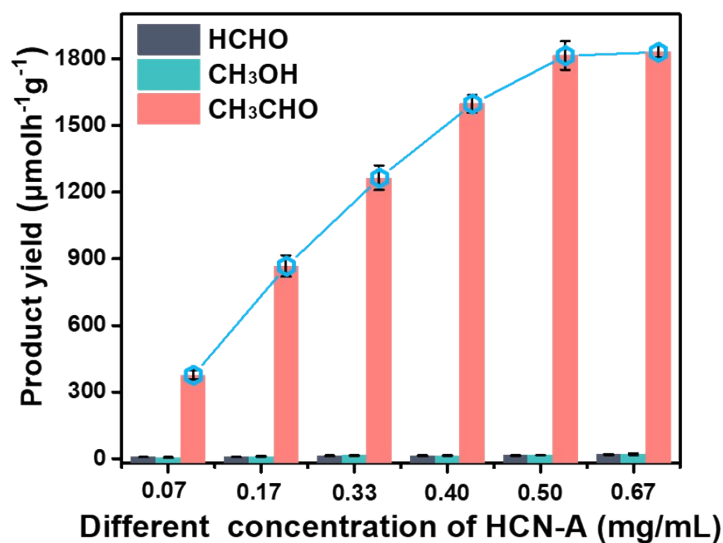


Figure S39. The product yield with different mass concentrations of HCN-A catalyst in 30 mL solvent at 10 °C in 30 mL.

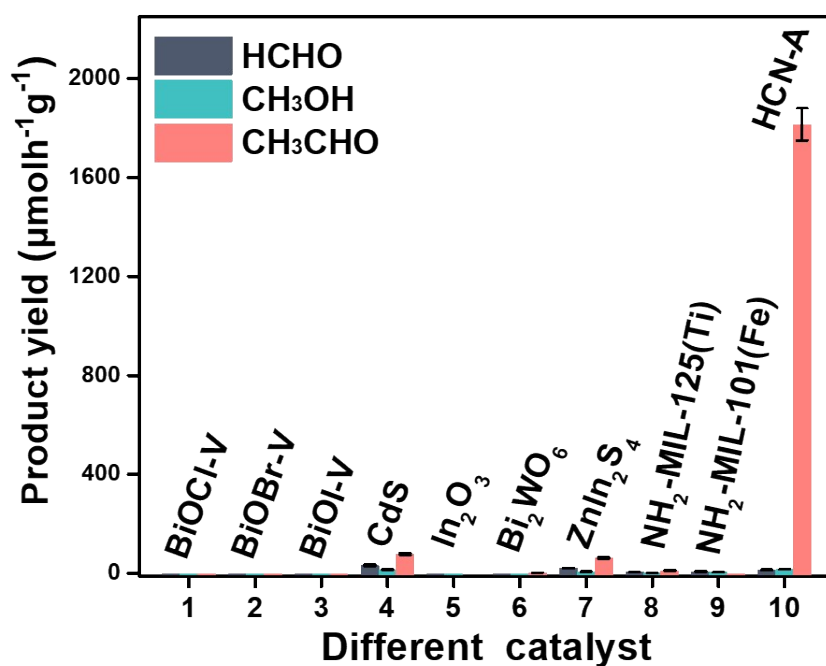


Figure S40. The generation rate of CO₂ reduction liquid products with different catalyst with the 30 mL solvent at the temperature of 10 °C, the catalyst including BiOCl-V, BiOBr-V^[15], BiOI-V, CdS^[16], In₂O₃^[17], Bi₂WO₆^[16], ZnIn₂S₄^[16], two kinds of reductive Metal–organic framework: NH₂-MIL-125 (Ti)^[18], NH₂-MIL-101 (Fe)^[19], and HCN-A. The above mentioned photocatalysts were prepared according to the cited papers.

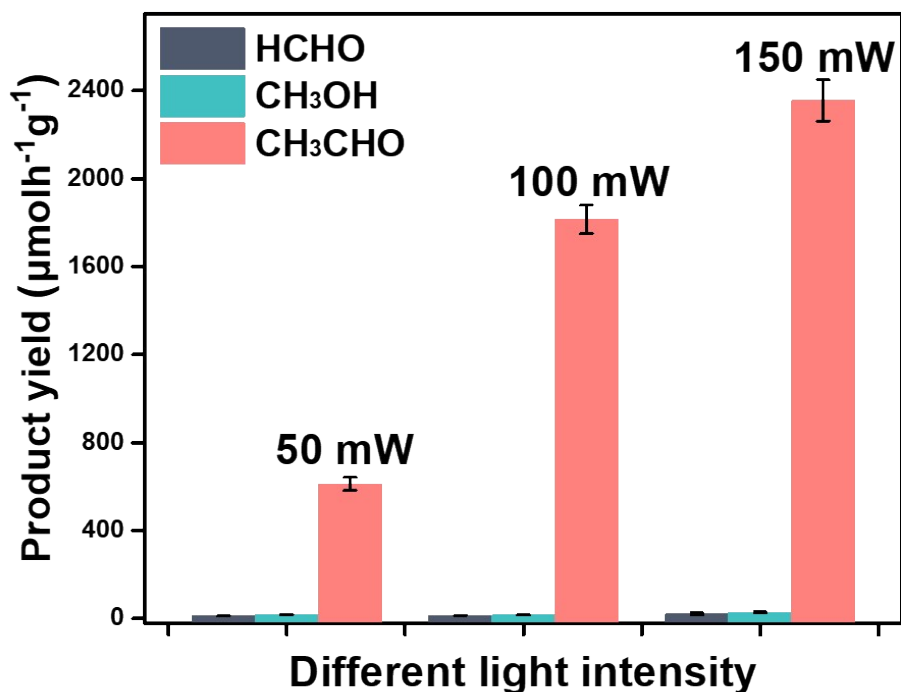


Figure S41. The generation rate of CO₂ reduction products under different incident light intensity of 50 mW, 100 mW and 150 mW cm⁻² by using HCN-A as the catalyst in 30 mL solvent at 10 °C.

Additional discussions:

The relationship between the activity performance and the light intensity was examined. With an increase in light intensity from 50 to 150 mW cm⁻² (Figure S41), the yields of CH₃CHO increased from 612.2 (50 mW cm⁻²) to 1814.7 (100 mW cm⁻²) and further achieved the yield of 2356.5 µmolh⁻¹g⁻¹ (150 mW cm⁻²). The result together with the mentioned control experiment demonstrate the successful conversion of CO₂ to CH₃CHO is driven by the light source.

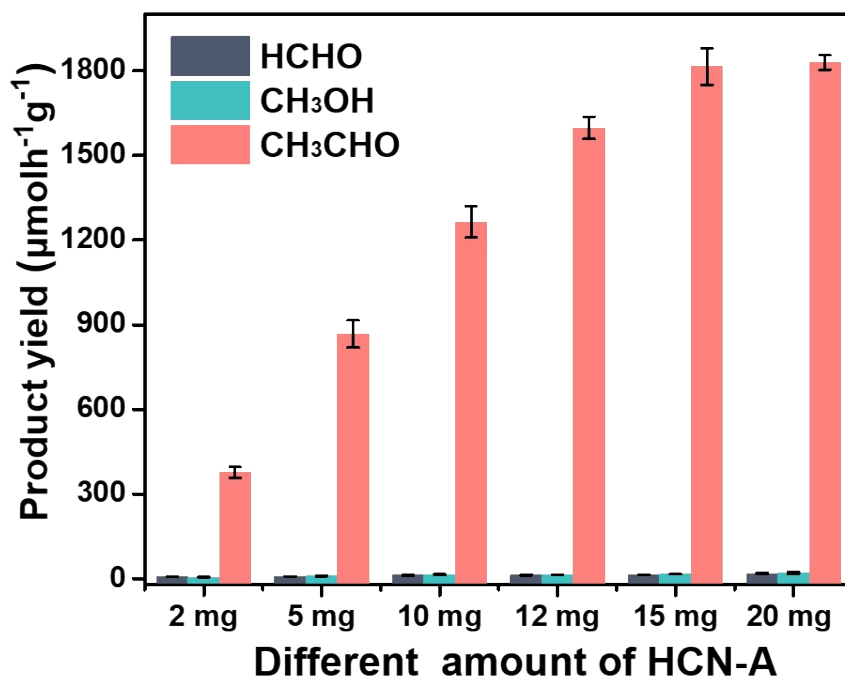


Figure S42. The generation rate of CO₂ reduction products with different amount of HCN-A catalyst with the 30 mL solvent at the temperature of 10 °C.

Additional discussions:

Note that the photocatalytic activity over the usage of different amount of HCN-A catalyst (Figure S42) suggests the 15 mg catalyst could almost absorb all the incident photon, therefore, this amount of catalyst was used for the calculation of QE.

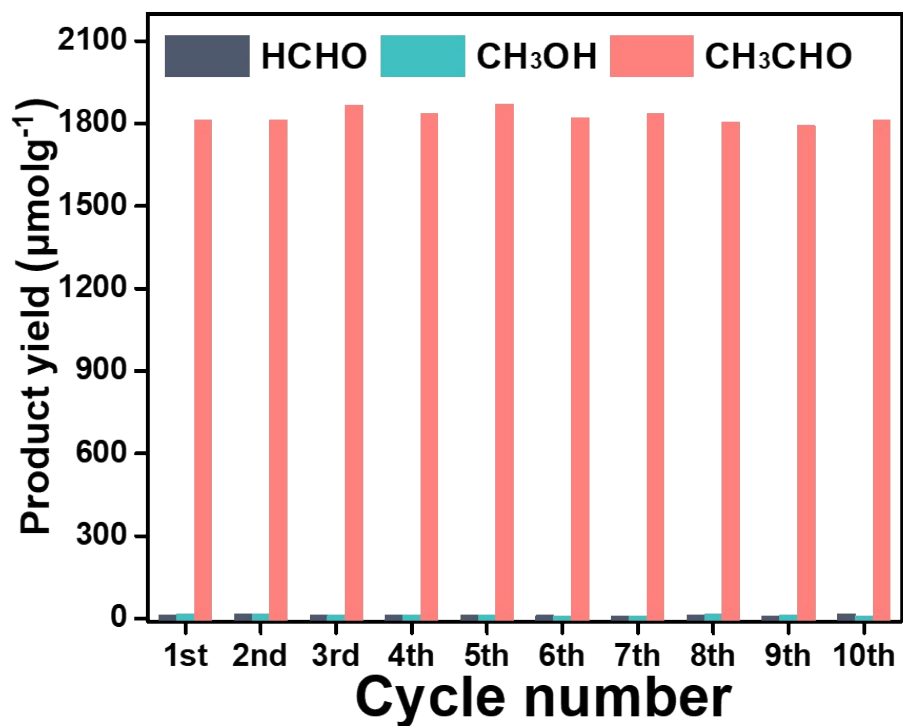


Figure S43. Stability experiments for photocatalytic CO₂ reduction using HCN-A.

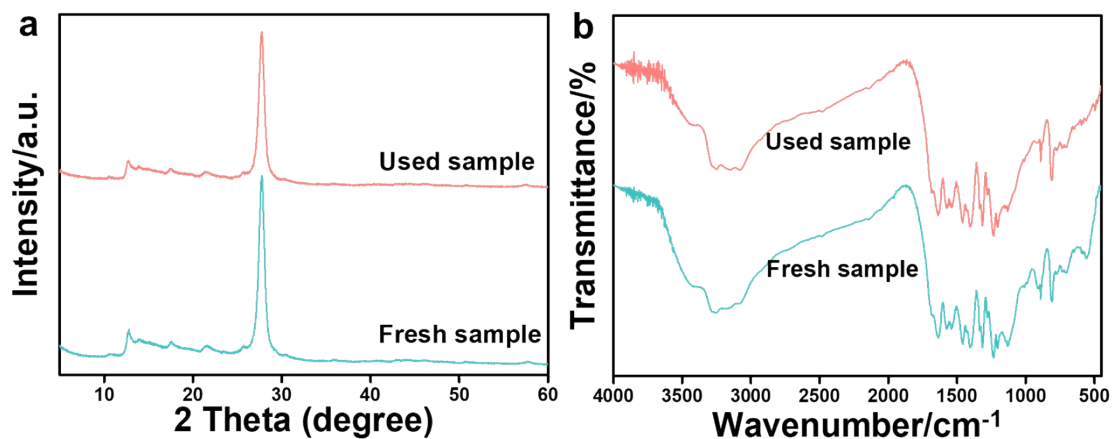


Figure S44. (a) XRD patterns and (b) FTIR spectra of the fresh and used HCN-A.

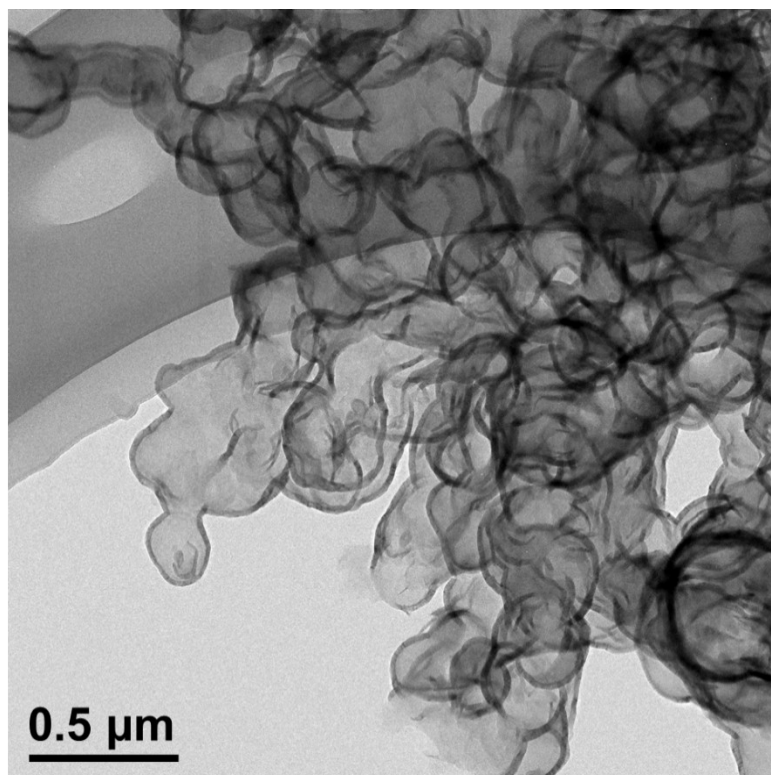


Figure S45. TEM image of the used HCN-A sample.

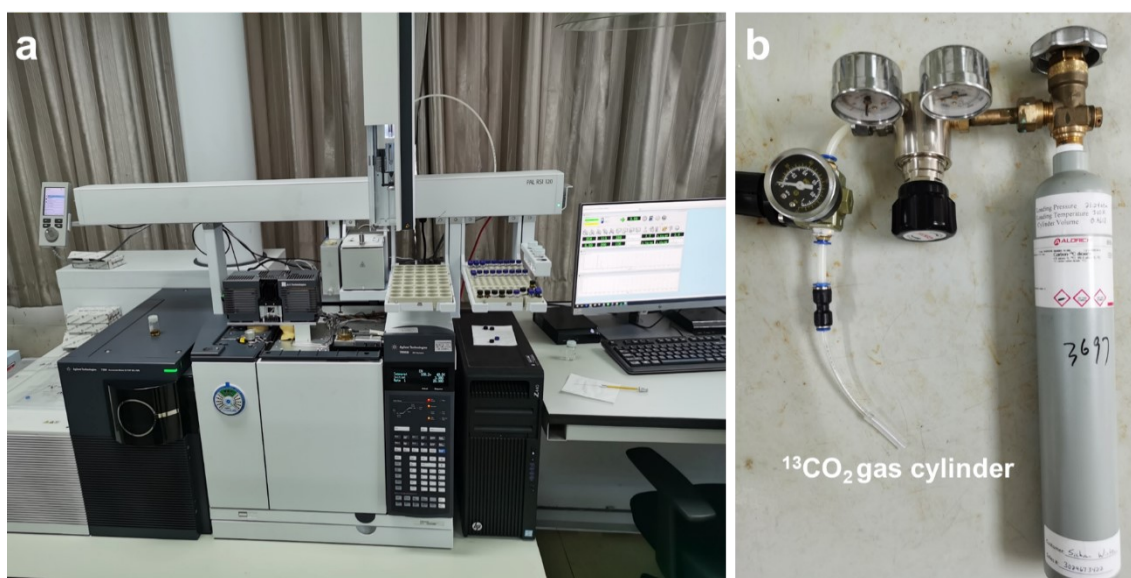


Figure S46. Digital picture of (a) Agilent Technologies 7890B-7250 Accurate-Mass Q-TOF GC/MS system for the isotope labeling experiment and (b) $^{13}\text{CO}_2$ gas cylinder.

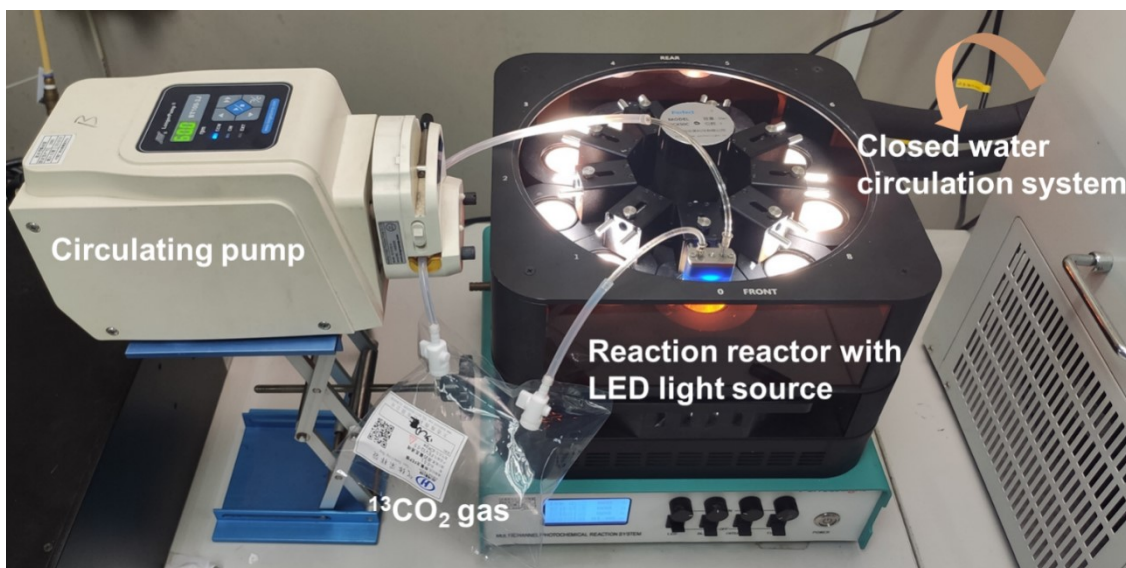


Figure S47. Digital picture of the device to do the isotope labeling experiment.

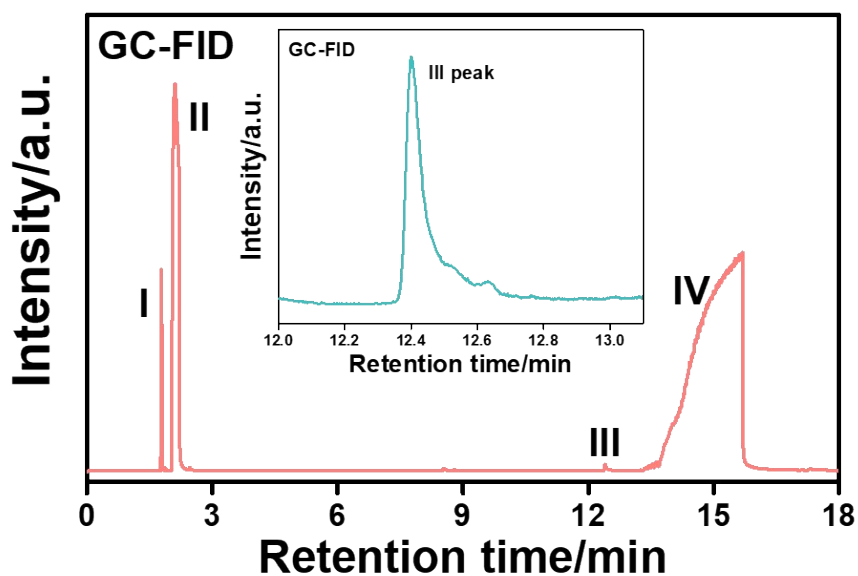


Figure S48. GC/FID signals for the CO₂ reaction solution after illumination for 1 h, footnote I, II, III, and IV represents the dissolved CO₂ species, acetonitrile, TEOA adducts, and TEOA derivative, inset figure is the enlargement peak III.

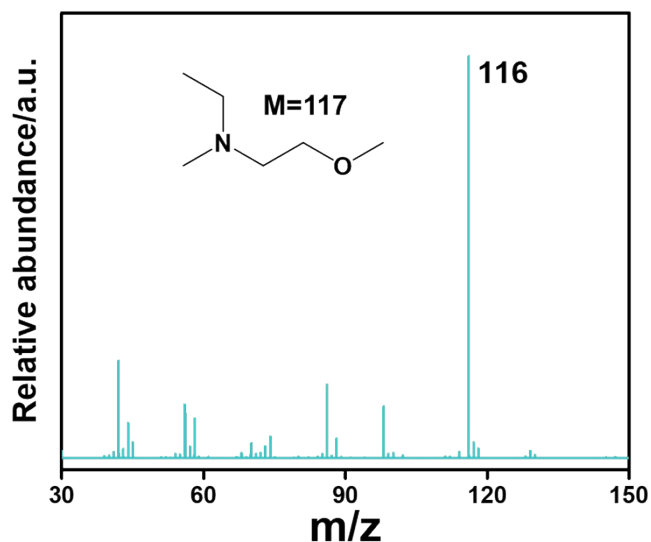


Figure S49. MS spectrum for the corresponding peak III from the GC/FID signal. Noted that the rectangle region III represents the sacrificial agent of TEOA.

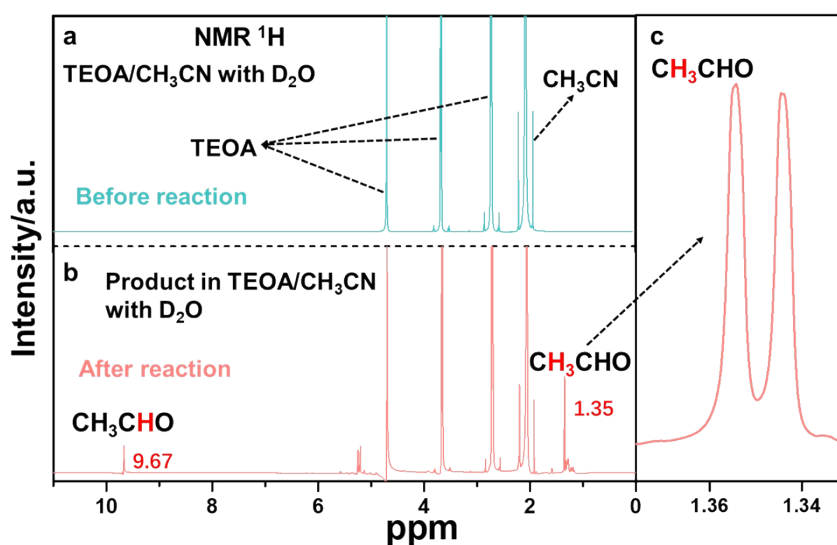


Figure S50. ¹H NMR spectral of (a) 0.1mL of (10%) TEOA/MeCN TEOA/MeCN (triethanolamine/acetonitrile) solvent before reaction in 0.5 mL D₂O. (b) 0.1 mL of the reaction solvent mixed with 0.5 mL D₂O, the reaction solvent was collected from the employed reaction system after 1 hour visible light illumination by using the HCN-A catalyst and under the CO₂ atmosphere. (c) the enlarged methyl hydrogen peak of CH₃CHO at 1.35 ppm in Figure R16b. Note that the liquid sample is stored at 10 °C before using the NMR analyzed with water suppression.

Additional discussions:

Figure S50a presents the the ^1H NMR of the reaction TEOA (10%)/MeCN solvent before illumination, both the MeCN and TEOA could be investigated. After illumination for 1 h (Figure S50b), two new peaks are generated and located at 1.35 ppm and 9.67 ppm of which corresponding to the methyl hydrogen ($-\text{CH}_3$) and aldehyde hydrogen ($-\text{CHO}$) in CH_3CHO product, respectively. Furthermore, it is observed the existence of two splitting peaks at 1.35 ppm (Figure S50c), further demonstrating the formation of methyl hydrogen ($-\text{CH}_3$). These NMR results verify the formation of CH_3CHO product.

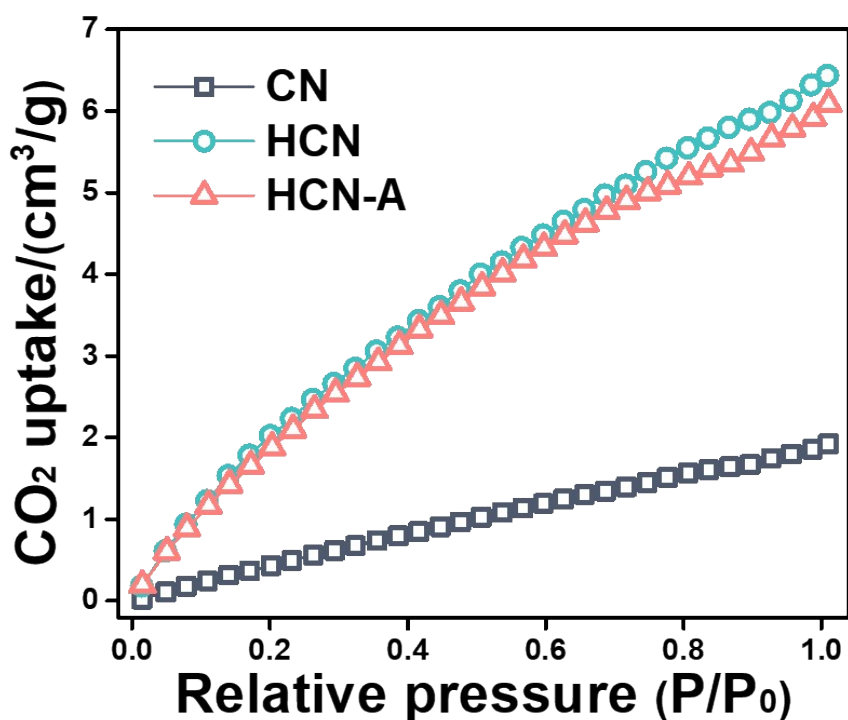


Figure S51. CO_2 adsorption isotherms of CN, HCN and HCN-A.

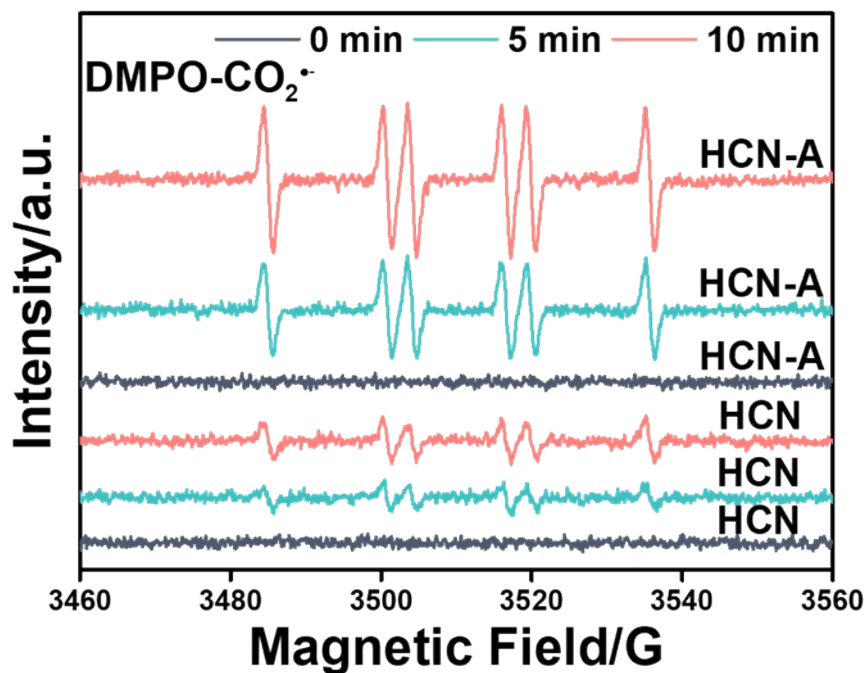


Figure S52. In-situ EPR spectra by using HCN-A or HCN as the catalyst, dispersed in TEOA/MeCN (triethanolamine/acetonitrile) solvent under the CO₂ atmosphere, 5,5-dimethyl-1-pyrroline-N-oxide (DMPO) was selected as the radical scavenger. The EPR spectra were collected from the 0 min (dark time), 5 min and 10 min under the visible light illumination.

Additional discussions:

The in-situ EPR measurement is used to detect the radical active species. Under the dark time, the EPR signal keeps silent in the CO₂ atmosphere. When the light is employed, the EPR signal of the characteristic DMPO-CO₂^{•-} adduct by using HCN-A is clearly presented, in line with previous literatures (Free Radic. Res.1995, 23:6, 593-614.; Toxicol. Lett. 1995, 82, 951-960.). This indicates the CO₂ molecules is able to be activated into the CO₂^{•-} radical under the light illumination. The CO₂ to CO₂^{•-} process is then followed by the generation of the important ^{*}CO intermediate, the prerequisite for the CO₂ conversion to the final CH₃CHO products. And the intensity of DMPO-CO₂^{•-} EPR signal is gradually increased as with the extended irradiation time, demonstrating the well light-responsive capability. When compared to the HCN-A, the use of HCN catalyst could also generate the CO₂^{•-} radical under the light illumination, while, the intensity of DMPO-CO₂^{•-} EPR signal in HCN is obviously smaller than

applied HCN-A under the identical condition. This result could further manifest the HCN-A has a higher efficiency for the CO₂ conversion to CH₃CHO.

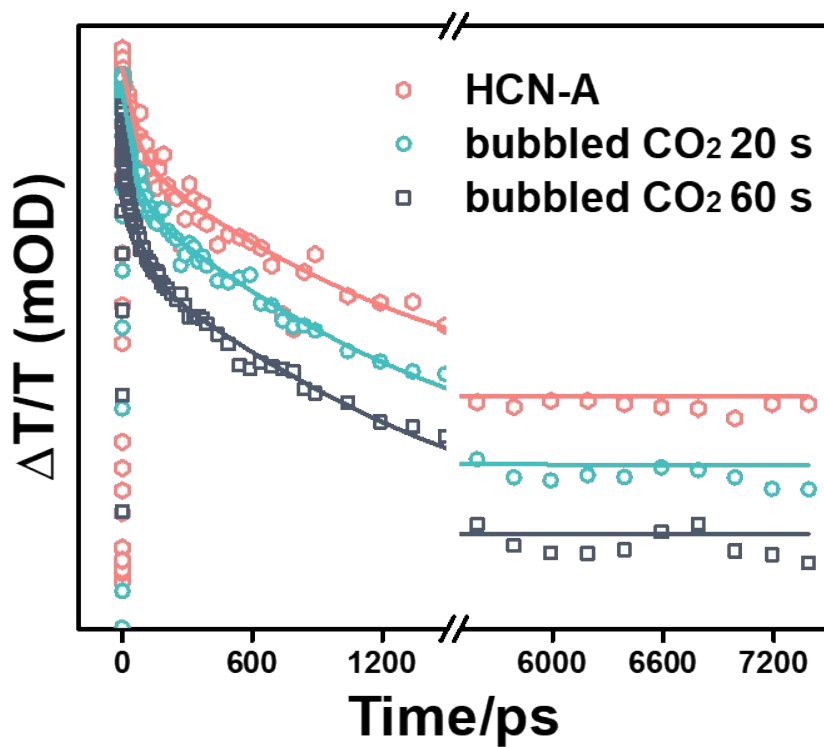


Figure S53. The comparison of femtosecond time-resolved transient absorption decay among the HCN-A catalyst suspension by bubbled the CO₂ 0 s, 20 s and 60 s.

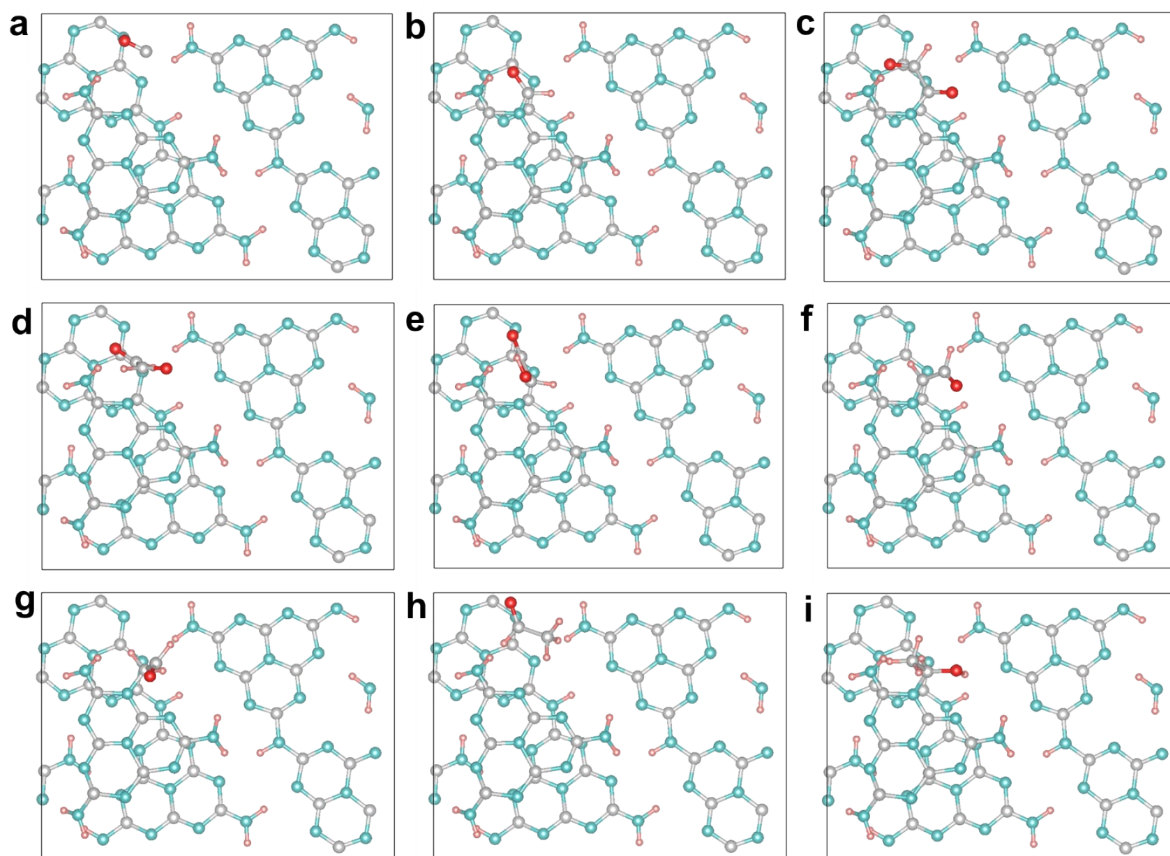


Figure S54. Calculated models of the reaction intermediates from the intermediate CO to CH_3CHO , (a) CO, (b) $^*\text{CHO}$, (c) $^*\text{OCCHO}$, (d) $^*\text{OCHCHO}$, (e) $^*\text{OCHCHOH}$, (f) $^*\text{OCHCH}$, (g) $^*\text{OCHCH}_2$, (h) $^*\text{OCHCH}_3$, and (i) $^*\text{OCH}_2\text{CH}_3$ on HCN-A, the reaction electron migration paths see the section of 1.6. Calculation of quantum efficiency (QE). The grey, blue, red, and green color sphere denote the carbon, nitride, oxygen, and hydrogen atom respectively.

4. Tables

Table S1. Specific surface areas, pore volumes, and band gaps of CN, HCN, HCN-A₁, HCN-A₂, HCN-A₃ and HCN-A₄.

Entry	Sample	S ^a (m ² g ⁻¹)	Fold Enhancem ent	PV ^b (cm ³ g ⁻¹)	Fold Enhancem ent	Band Gap (eV)
1	CN	14.2	1	0.07	1	2.71
2	HCN	94.4	6.65	0.31	4.43	2.87
3	HCN-A ₁	89.3	6.29	0.30	4.29	2.77
4	HCN-A ₂	86.4	6.08	0.30	4.29	2.72
5	HCN-A ₃	81.6	5.75	0.28	4.00	2.59
6	HCN-A ₄	75.1	5.29	0.26	3.71	2.52

S^a: specific surface area; PV^b: pore volume

Table S2. Surface C/N mole ratios of all the samples as determined by XPS analysis.

Entry	Sample	C ^a	N ^a	C/N
1	CN	41.15	56.97	0.72
2	HCN	40.63	58.44	0.69
3	HCN-A ₁	40.96	58.00	0.71
4	HCN-A ₂	40.99	57.95	0.72
5	HCN-A ₃	41.98	57.61	0.73
6	HCN-A ₄	42.10	56.04	0.75

[a]: mole (atomic) conc (%)

Table S3. Organic elemental analysis of CN, HCN, HCN-A₁, HCN-A₂, HCN-A₃, and HCN-A₄.

Entry	Sample	C	N	H	C/N ^a
		[wt%]	[wt%]	[wt%]	mol%
1	CN	34.25	57.63	2.43	0.69
2	HCN	31.37	57.60	2.76	0.63
3	HCN-A ₁	31.81	56.81	2.72	0.65
4	HCN-A ₂	32.58	56.79	2.57	0.67
5	HCN-A ₃	33.62	56.04	2.12	0.70
6	HCN-A ₄	34.89	55.68	2.15	0.73

C/N^a: mole ratio of C/N

Table S4. Relative ratios of C-N=C, N-(C)₃, and C-N-H of CN, HCN, HCN-A (HCN-A₃) as determined from XPS N 1s spectra.

samples	C=N-C		N-(C) ₃		C-N-H		N-(C) ₃ / C=N-C
	BE ^a	ratio ^b	BE ^a	ratio ^b	BE ^a	ratio ^b	
CN	398.7	49.2	399.2	32.4	400.71	18.4	0.66
HCN	398.7	49.1	399.1	32.1	400.77	18.8	0.65
HCN-A	398.7	44.7	399.0	36.6	400.75	18.7	0.81

BE^a: Bind Energy; **ratio^b:** calculated area ratio versus the total area;

Table S5. Product yield and CH₃CHO selectivity of CN, HCN, HCN, HCN-A₁, HCN-A₂, HCN-A₃, and HCN-A₄ with the 3 mL solvent or 30 mL solvent.

Entry	Sample	CH ₃ CHO ^a	Selectivity/% ^a	CH ₃ CHO ^b	Selectivity/ % ^b
1	CN	22.3	47.3	33.9	49.5
2	HCN	145.3	51.6	230.7	54.7
3	HCN-A ₁	198.8	62.6	340.1	67.2
4	HCN-A ₂	499.6	87.8	874.6	91.5
5	HCN-A ₃	1083.5	95.5	1814.7	98.3
6	HCN-A ₄	893.1	94.7	1364.4	96.4

^a: (μmolh⁻¹g⁻¹), 3 mL solvent; ^b: (μmolh⁻¹g⁻¹), 30 mL solvent;

Table S6. The data of action spectra and quantum efficiency (QE) of CH₃CHO generation under incident light with different wavelengths by using HCN-A.

Entry	λ/nm	CH ₃ CHO ^a	N _e ^b	E _s /J	I ^c	N _p ^d	AQE/%
1	365	17.64	4.901	5.449×10 ⁻¹⁹	10.1	2.031×10 ⁻⁷	24.13
2	385	12.97	3.603	5.167×10 ⁻¹⁹	7.6	1.612×10 ⁻⁷	22.35
3	420	23.07	6.409	4.736×10 ⁻¹⁹	20.9	4.837×10 ⁻⁷	13.25
4	450	18.50	5.140	4.420×10 ⁻¹⁹	23.6	5.852×10 ⁻⁷	8.78
5	485	12.49	3.469	4.101×10 ⁻¹⁹	20.2	5.398×10 ⁻⁷	6.43
6	535	3.11	0.863	3.718×10 ⁻¹⁹	9.8	2.889×10 ⁻⁷	2.99
7	595	0.57	0.158	3.343×10 ⁻¹⁹	5.6	1.836×10 ⁻⁷	0.86
8	630	0.34	0.096	3.157×10 ⁻¹⁹	14.5	5.034×10 ⁻⁷	0.19

CH₃CHO^a: (generation rate/μmolh⁻¹); N_e^b: ×10⁻⁸ mols⁻¹; I^c: mW/cm²; N_p^d: mols⁻¹;

Table S7. The data of action spectra and apparent quantum efficiency (AQE) of CH₃CHO generation under incident light with different wavelengths by using HCN.

Entry	λ/nm	CH ₃ CHO ^a	N _e ^b	E _s /J	I ^c	N _p ^d	AQE/%
1	365	4.108	1.141	5.449×10 ⁻¹⁹	10.1	2.031×10 ⁻⁷	5.62
2	385	2.606	0.724	5.167×10 ⁻¹⁹	7.6	1.612×10 ⁻⁷	4.49
3	420	4.475	1.243	4.736×10 ⁻¹⁹	20.9	4.837×10 ⁻⁷	2.57
4	450	1.960	0.544	4.420×10 ⁻¹⁹	23.6	5.852×10 ⁻⁷	0.93
5	485	0.932	0.259	4.101×10 ⁻¹⁹	20.2	5.398×10 ⁻⁷	0.48
6	535	0.021	0.006	3.718×10 ⁻¹⁹	9.8	2.889×10 ⁻⁷	0.02
7	595	0	0	3.343×10 ⁻¹⁹	5.6	1.836×10 ⁻⁷	0.00
8	630	0	0	3.157×10 ⁻¹⁹	14.5	5.034×10 ⁻⁷	0.00

CH₃CHO^a: (generation rate/μmolh⁻¹); N_e^b: ×10⁻⁸ mols⁻¹; I^c: mW/cm²; N_p^d: mols⁻¹;

Table S8. Photocatalytic CO₂ reduction performances with CH₃CHO as one of the major products in previous reported photocatalysts in the literature, compared with that of HCN-A.

Entry	Catalyst	co-catalyst	R _{max} ^[a]	Selectivity	AQE (%) ^[b]	isotope labelling	DFT	Light source	Ref
1	HCN-A		1814.7	98.3%	13.26	¹³ CO ₂ /C ¹⁸ O ₂ / D ₂ O	Whole reaction	white LED light	This work
2	TiO ₂	Pd/Rh	0.21	67.7%	N.A.	N.A.	N.A.	UV light	20
3	InTaO ₄	NiO	0.32	N.A.	N.A.	N.A.	N.A.	UV light	21
4	C-SnS ₂		139	N.A.	0.72	¹³ CO ₂	CO ₂ absorption	300W, Hg-lamp	22
5	Graphene oxide/Cu		3.88	56.9%	N.A.	N.A.	N.A.	visible light	23
6	TiO ₂	V	11.13	69.6%	N.A.	N.A.	N.A.	UV light	24
7	Zn _x Cd _{1-x} S		15	63.8%	N.A.	N.A.	N.A.	300 W Xe-lamp	25
8	ZnFe ₂ O ₄		57.8	80.8%	N.A.	N.A.	N.A.	300 W Xe-lamp	26
9	Cu ₂ O		8.2	29.9%	N.A.	N.A.	N.A.	300 W Xe-lamp	27
10	TiO ₂	Rh	0.57	79.4%	N.A.	N.A.	N.A.	UV light	28
11	Nb-TiO ₂		572	98.1%	N.A.	N.A.	N.A.	UV light	29

[a] R_{max}: the best evolution rate of CH₃CHO generation, μmol•h⁻¹• g⁻¹; [b] The monochromatic wavelengths is applied at λ= 420 nm.

5. References

1. Q. Liu, H. Cheng, T. Chen, T. W. B. Lo, J. Ma, A. Ling, F. Wang, *Appl. Catal., B.* 2021, **295**, 120289.
2. A. Kudo, Y. Miseki, *Chem. Soc. Rev.* 2009, **38**, 253-278.
3. E. Bertheussen, A. Verdaguer-Casadevall, D. Ravasio, J. H. Montoya, D. B. Trimarco, C. Roy, S. Meier, J. Wendland, J. K. Nørskov, I. E. L. Stephens, I. Chorkendorff, *Angew. Chem. Int. Ed.* 2016, **55**, 1450-1454.
4. G. Kresse, J. Furthmüller, *Comput. Mater. Sci.* 1996, **6**, 15-50.
5. J. P. Perdew, K. Burke, M. Ernzerhof, *Phys. Rev. Lett.* 1996, **77**, 3865.
6. G. Kresse, D. Joubert, *Phys. Rev. B* 1999, **59**, 1758.
7. S. Grimme, J. Antony, S. Ehrlich, H. Krieg, *J. Chem. Phys.* 2010, **132**, 154104.
8. P. Makuła, M. Pacia, W. Macyk, *J. Phys. Chem. Lett.* 2018, **9**, 6814-6817.
9. D. Zhao, Y. Wang, C.-L. Dong, Y.-C. Huang, J. Chen, F. Xue, S. Shen, L. Guo, *Nat. Energy.* 2021, **6**, 388-397.
10. D. Zhao, C.-L. Dong, B. Wang, C. Chen, Y.-C. Huang, Z. Diao, S. Li, L. Guo, S. Shen, *Adv. Mater.* 2019, **31**, 1903545.
11. Q. Liu, C. Chen, K. Yuan, C. D. Sewell, Z. Zhang, X. Fang, Z. Lin, *Nano Energy* 2020, **77**, 105104.
12. K. Damodaran, G. J. Sanjayan, P. R. Rajamohanan, S. Ganapathy, K. N. Ganesh, *Org. Lett.* 2001, **3**, 1921-1924.
13. X. Xiao, Y. Gao, L. Zhang, J. Zhang, Q. Zhang, Q. Li, H. Bao, J. Zhou, S. Miao, N. Chen, J. Wang, B. Jiang, C. Tian, H. Fu, *Adv. Mater.* 2020, **32**, 2003082.
14. J. Yang, Z. Zeng, J. Kang, S. Betzler, C. Czarnik, X. Zhang, C. Ophus, C. Yu, K. Bustillo, M. Pan, J. Qiu, L.-W. Wang, H. Zheng, *Nat. Mater.* 2019, **18**, 970-976.
15. J. Di, J. Xia, M. F. Chisholm, J. Zhong, C. Chen, X. Cao, F. Dong, Z. Chi, H. Chen, Y.-X. Weng, J. Xiong, S.-Z. Yang, H. Li, Z. Liu, S. Dai, *Adv. Mater.* 2019, **31**, 1807576.
16. M. Wang, M. Liu, J. Lu, F. Wang, *Nat. Commun.* 2020, **11**, 1083.
17. Y.-X. Pan, Y. You, S. Xin, Y. Li, G. Fu, Z. Cui, Y.-L. Men, F.-F. Cao, S.-H. Yu, J. B. Goodenough, *J. Am. Chem. Soc.* 2017, **139**, 4123-4129.
18. H. Liu, J. Zhang, D. Ao, *Appl. Catal., B.* 2018, **221**, 433-442.
19. D. Wang, R. Huang, W. Liu, D. Sun, Z. Li, *ACS Catal.* 2014, **4**, 4254-4260.
20. O. Ola, M. Maroto-Valer, D. Liu, S. Mackintosh, C.-W. Lee, J. C. S. Wu, *Appl. Catal., B.* 2012, **126**, 172-179.
21. P.-Y. Liou, S.-C. Chen, J. C. Wu, D. Liu, S. Mackintosh, M. Maroto-Valer, R. Linforth, *Energy Environ. Sci.* 2011, **4**, 1487-1494.
22. I. Shown, S. Samireddi, Y.-C. Chang, R. Putikam, P.-H. Chang, A. Sabbah, F.-Y. Fu, W.-F. Chen, C.-I. Wu, T.-Y. Yu, P.-W. Chung, M. C. Lin, L.-C. Chen, K.-H. Chen, *Nat. Commun.* 2018, **9**, 169.
23. I. Shown, H.-C. Hsu, Y.-C. Chang, C.-H. Lin, P. K. Roy, A. Ganguly, C.-H. Wang, J.-K. Chang, C.-I. Wu, L.-C. Chen, K.-H. Chen, *Nano Lett.* 2014, **14**, 6097-6103.
24. O. Ola, M. M. Maroto-Valer, *Chem. Eng. J.* 2016, **283**, 1244-1253;
25. L. Tang, L. Kuai, Y. Li, H. Li, Y. Zhou, Z. Zou, *Nanotechnology* 2018, **29**, 064003.
26. J. Xiao, W. Yang, S. Gao, C. Sun, Q. Li, *J. Mater. Sci. Technol.* 2018, **34**, 2331-2336.

27. M. L. Ovcharov, A. M. Mishura, N. D. Shcherban, S. M. Filonenko, V. M. Granchak, *Sol. Energy*. 2016, **139**, 452-457.
28. C.-W. Lee, R. Antoniou Kourounioti, J. C. S. Wu, E. Murchie, M. Maroto-Valer, O. E. Jensen, C.-W. Huang, A. Ruban, *J. CO2 Util.* 2014, **5**, 33-40.
29. X. Qian, W. Yang, S. Gao, J. Xiao, S. Basu, A. Yoshimura, Y. Shi, V. Meunier, Q. Li, *ACS Appl. Mater. Interfaces*. 2020, **12**, 55982-55993.